MASTER'S THESIS

Finding The Dark Gas in The Milky Way

A thesis submitted to the University of Manchester for the degree Master of Science by Research in Astrophysics and Astronomy

in the

Department of Physics and Astronomy in the School of Natural Sciences
Faculty of Science and Engineering

2022

Author
Rathan Makam Pandu Ranga Setty

Supervisors
Prof. Gary A Fuller
Dr. Rowan J Smith

Contents

List of Figures

List of Tables

.

THE UNIVERSITY OF MANCHESTER

Abstract

Faculty of Science and Engineering
Department of Physics and Astronomy in the School of Natural Sciences

Master of Science by Research in Astrophysics and Astronomy

Finding The Dark Gas in The Milky Way

by

Rathan Makam Pandu Ranga Setty

The interstellar medium is the medium that occupies the space between stars, and it is the host for new star formation. Molecular hydrogen H_2 is the most abundant molecule of interstellar gas. However, due to the lack of permanent dipole moment, the H_2 cannot be detected directly and is traced by the second most abundant molecule CO. H_2 self-shields itself from UV radiation. In contrast, the CO fails to self-shield itself, and the gas phase carbon will be present in C or C^+. Thus, some amount of H_2 has not been traced by CO, known as "CO-dark gas". $10M_\odot$ resolution region of the fiducial Milky Way model, which is produced by the high-resolution simulations using a moving AREPO code, has been adopted to perform this thesis which aims to investigate the amount of CO-dark gas mass present in this region at 50pc, 100pc,250pc,500pc, and 1kpc spatial resolution of the AREPO image.

It is observed that as the spatial resolution is increased, more CO is detected for H_2 column densities $\geq 10^{20}$ cm^{-2}. This affects the globally averaged CO-H_2 conversion factor (X_{CO}) up to a factor of 3. The standard value for CO integrated intensity threshold ($W_{CO,th}$, threshold to distinguish between CO dark and CO bright gas) less than 10 K kms^{-1} does not hold good for 50pc, 100pc, and 250pc spatial resolutions. At these spatial resolutions, CO tends to be bright before reaching the $W_{CO,th}$ and new CO integrated intensity threshold ($W_{CO,newth}$) less than 1 K kms^{-1} provides the better estimation of CO-dark gas fraction. CO-dark gas fraction varies along with the spatial resolution of the AREPO image. At high resolution, we miss 1% - 34% (50pc), 15% - 32% (100pc), 10% - 24% (250pc), 22%(500pc) and 36%(1kpc) of H_2 mass the $10M_\odot$ resolution region. For the sub-regions, the amount of H_2 mass that is missed varies on the spatial resolution.

CO-dark gas fraction found at 10^{15} cm$^{-2} < N_{CO} < 10^{17}$ cm^{-2}, 10^{18} cm$^{-2} < N_{H_2}$

$< 10^{22}$ cm^{-2}, 10^{20} cm$^{-2} < N_{HI} < 10^{22}$ cm^{-2} and 10^{20} cm$^{-2} < N_{SD} < 10^{22}$ cm^{-2} for all the spatial resolutions, but at the poor spatial resolution the CO-dark gas fraction is obscured. A huge scatter is observed along with these column densities in the CO-dark gas distribution. By the use of box plots where CO-dark gas fraction is limited to a maximum of 0.98, it is found that in the binned intervals of $10^{0.5}$ cm^{-2} in the range (which is stated above) for N_{H_2}, N_{HI}, N_{SD} the CO-dark gas fraction distribution is both left and right skewed showing no uniform variations in the mean CO-dark gas fractions of the binned column densities. For a given column density, the mean of CO-dark gas fraction varies at different spatial resolutions. Hence, no correlation is found between CO-dark gas fraction and either of N_{H_2}, N_{HI} or N_{SD}.

CO-H_2 conversion factor also varies depending on the spatial resolution as more CO is detected at high spatial resolutions. However, at low N_{H_2} each subregions have high globally averaged X_{CO} values and decreases as N_{H_2} increases. Nevertheless, X_{CO} is sensitive to the spatial resolution for a given N_{H_2}.

Declaration of Authorship

No portion of the work referred to in this thesis has been submitted in support of an application for another degree or qualification of this or any other university or other institution of learning.

Copyright Statement

Chapter 1

Introduction

1.1 Interstellar Medium

The space between stars seemed empty, i.e., the dark patches in between the stars in the photographic atlas of the Milky Way by E.E.Barnard. However, these dark patches seemed not to be empty; instead, the light by stars(starlight) was obscured by the dust present between them. This process is known as "Interstellar Reddening". Thus, the space between the stars was concluded not to be empty; instead consists of a medium known as "Interstellar Medium"(ISM). Similarly, the medium between the galaxies is known as the "Inter-Galactic Medium." (IGM) (Kwok (2007)). Hydrogen is the main constituent of ISM (70%) followed by Helium (28%), heavier atoms (1%), and remaining is the dust(1%) which is mainly a composition of silicates (Si, O, H), oxides (O, Fe, Al), icy mantles (H_2O, CO, CO_2) and carbonaceous (C, H, N) materials in the solid phase (Cartagena (2020)).

Being the medium between stars, the interstellar medium is also the birthplace of stars. The interstellar medium is the vault of ashes of previous generation stars, boosted by the products of nucleosynthesis produced during star's evolution. The nucleosynthesis products are injected into the interstellar medium either by a supernova explosion or by stellar winds. As the nucleosynthesis products are injected more and more, the interstellar medium becomes richer (an increase of abundance) of heavier elements which is a part of the stellar evolution of a galaxy, and thus interstellar medium becomes the progenitor of new stars(Tielens (2010)).

A continual flow of energy through the interstellar medium and the interchange of materials within itself and stars form a cycle and drives the evolution of the galaxy (Burton et al. (2013)). Some part of interstellar gas from the intergalactic medium (IGM) is added to the interstellar medium, which increases its

mass. Table 1.1 show that interstellar medium exists as a multiphase medium that differs in density and temperature and the nature of the constituents.

TABLE 1.1: Multiphase ISM (Draine (2011))

Medium	Temperature(K)	Density(cm^{-3})	Properties
Hot Ionized Medium (HIM)	$> 10^{5.5}$	0.004	Shock waves heat the gas, and ionization is due to collision with OVI ions.
Warm Ionized Medium (WIM)	10^4	0.3-10^4	Hydrogen Gas is heated by ultraviolet photons produced by the newborn O-type stars
Warm Neutral Medium (WNM)	~ 5000	0.6	Hydrogen is found in neutral form with a small fraction of ionization
Cold Neutral Medium (CNM)	~ 100	30	Dense with hydrogen in the neutral form
Diffuse molecular gas	~ 50	~ 100	Similar to CNM but with large column densities, providing self-shielding of hydrogen
Dense Molecular Gas	10-50	$10^3 - 10^6$	Found in gravitationally bound clouds with very high densities consisting of dust grains coated with mantles. Star formation occurs in these clouds

The interstellar medium matter is diversely distributed in well-defined phases. The interstellar medium has multiphase because it is not stationary, and due to the interstellar medium being dynamic, the baryons undergo several changes from one phase to another, like ionizing photons from stars, which can ionize the cold molecular gas to hot ionized hydrogen (HII) and similarly, radiative cooling can allow hot ionized gas to cool at low temperatures, where ions and electrons can recombine to form atoms and further atoms can recombine to form a H_2 molecule.

The naked eye cannot directly detect the matter present in the interstellar medium. The emission or absorption of radiation by atoms, ions, or molecules present in interstellar gas is used to observe the interstellar medium. In an interstellar medium (ISM) the stars are formed in Giant Molecular Clouds (GMCs). The name itself suggests that it is entirely molecular. It cannot be said that all GMCs form stars, but at least it is scarce in the solar vicinity of the non-star-forming GMCs to be found. Appearing as descriptive and having precise boundaries

are the main description of GMCs, and they are gravitationally bound. Though it is known that star formation occurs in GMCs, the formation and what precisely a GMC has is yet to have a generally accepted definition. There is a small amount of variance regarding the classification of a giant cloud as GMC, but it is unaccepted, including all the definitions of GMC(Blitz (1993)). Having precise boundaries suggests that at the edges of the molecular cloud, there is an occurrence of phase transition. It is apparent that a molecular cloud is associated with atomic hydrogen envelopes of the same mass as the molecular cloud. For the complete description and details of formation GMC (see Blitz (1993) and Pringle et al. (2001)).

1.2 Hydrogen

As stated in 1.1, hydrogen is the most abundant element in the interstellar medium. So, understanding the physics of hydrogen and its phases is of great importance to understanding the process in the interstellar medium. The discovery of spectral lines from H^+, H-atoms, H_2 molecules, $H_2{}^+$ and $H_3{}^+$ from the interstellar medium has made a significant impact in the study of ISM (Islam (2010)).

1.2.1 Early Universe Hydrogen

In the period known as the "Recombination Era", i.e., after 3×10^5 years after the Big Bang, the first hydrogen and helium atoms were formed by electrons and protons. Ever since, the formation of hydrogen in atomic and molecular forms has showcased itself in the primary role of shaping the universe. After the Big Bang, the universe was extremely hot, around 1000K, under which the hydrogen atoms can ionize and radiate the heat once cooled. This leads to the gravitational collapse to form stars and galaxies. Cooling of gas is an important mechanism that allows gravitational collapse as the effect of the pressure of the hot gas resisting any more contraction unless the heat is radiated away.
Once the neutral hydrogen is formed, the molecular ions such as $H_2{}^+$ and HD were formed due to radiative reactions. Ion-Molecule exchange reaction, which includes electrons and protons, leads to forming of the first hydrogen molecule (H_2). A typical ion-molecule exchange reaction is as follows: (Islam (2010)):

$$\begin{aligned} H + e^- &\rightarrow H^- + h\nu \\ H^- + H &\rightarrow H_2 + e^- \end{aligned} \tag{1.1}$$

or

$$\begin{aligned} H + H^+ &\rightarrow {H_2}^+ + h\nu \\ {H_2}^+ + H &\rightarrow H_2 + H^+ \end{aligned} \tag{1.2}$$

1.2.2 Neutral Atomic Hydrogen(HI)

Hydrogen in the form of neutral atomic is the form in which the interstellar medium in the disk of galaxies is present. Neutral atomic hydrogen gas can be present in thermal equilibrium at temperatures less than few 100K, known as Cold Neutral Medium (CNM), and at temperatures less than a few 1000K, which is known as Warm Neutral Medium (WNM). In the interstellar medium, neutral atomic hydrogen is a two-phase medium where CNM and WNM can co-exist in pressure equilibrium. The electron's spin in the electronic ground state of a hydrogen atom can be parallel or antiparallel, with higher and lower energy levels, respectively. The magnetic fields of electron and proton, which are produced due to the spins, form a coupling that results in the "hyperfine splitting" of the hydrogen atom. When an electron returns to its ground state, a photon of wavelength λ = 21.1 cm is emitted. The spectral line of this wavelength is known as the 21 cm line, which is uniquely emitted by HI. Hence, neutral atomic hydrogen (HI) is detected by this spectral line. The distribution of this form of hydrogen in the interstellar medium is referred to as "HI regions". The number density n(HI) is 1 atom cm^{-3}. More than 95 percent of the interstellar medium is probably believed to be in hydrogen and helium neutral phases(Spitzer (1998)). The study of a 21 cm line from atomic hydrogen has been a significant impact in mapping the HI distribution in Milky Way and other galaxies (Draine (2011)). In the Interstellar medium, atomic hydrogen (HI) is present in Warm Neutral Medium(WNM) and Cold Neutral Medium(CNM), where the cooling processes are by optical line and fine-structure line emission for WNM and only fine-structure line emission for CNM (Draine (2011)).

1.2.3 Ionised Hydrogen

The most luminous, most massive, and with high surface temperatures, stars like types O and B release an ultraviolet photon during their evolution with energies higher than 13.6ev (ionization energy for hydrogen). So, as the released photon reaches, the hydrogen atoms surrounding or present near the stars are ionized, and this process of ionization is known as photoionization. The region of such

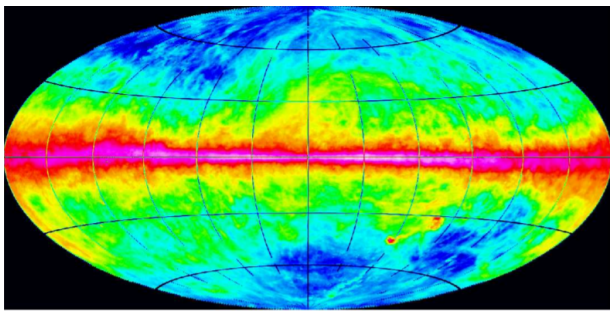

FIGURE 1.1: All sky HI 21 cm line intensity from LAB survey. The Galactic centre is in the middle (Kalberla et al. (2005))

ionized hydrogen is known as the "HII region". The radio-recombination lines and emissions at different wavelengths like the Balmer lines and the Balmer continuum, continuum emission at infrared and radio frequencies are used to study the HII regions (Spitzer (1998)). During the star's lifetime, which is responsible for ionization, the HII regions do not tend to travel more from the regions where they are formed. Hence, studying HII regions is of great importance to understanding the ISM. The ionizing photons from O and B stars escape these HII regions and are responsible for the ionization in a Warm Ionized Medium (WIM) (Luisi (2019)).

FIGURE 1.2: The Trifid Nebula (M20). A single O7 star powers the optical image of an HII region. The bright region is the HII region (red) in Hα, and the starlight scattered by dust is the blue haze in the North (Draine (2011)). The image is taken from Astronomy Picture of the Day.https://apod.nasa.gov/apod/ap210812.html

1.2.4 Molecular Hydrogen

Hydrogen in the molecular form (H_2) is the most abundant molecule in the universe (Draine (2011)), which is the dominant molecule of the mass budget of gas in star-forming regions (Cazaux & Tielens (2002)). Star formation occurs in denser and cold molecular clouds, where the transformation of atomic gas (diffuse) to molecular gas (dense) is considered the most crucial step in the star formation process in ISM (Busch et al. (2019a)). As the transformation is essential in the cooling mechanism of the interstellar medium, it regulates the star formation in galaxies (Glover & Abel (2008)). It is expected that there is a possibility of the very first generations of stars, molecular gas fuels the star formation (Bolatto et al. (2013))

The theory of the formation of molecular hydrogen in the interstellar medium that is widely accepted is the formation of H_2 on the surface of the dust grains in the interstellar medium via heterogeneous catalysis. Van de Hulst first suggested this in 1948, and Salpeter and Gould modeled it in 1963. In this type of formation, all the H-atoms that are absorbed into the dust grains leave as part of a H_2, and hence this process is thought to be highly efficient. In this process, the molecular hydrogen may be formed in three ways: i) The absorbed H-atom on the dust grain surface is reacted with another H-atom, which is still in the gas phase, and molecular hydrogen (H_2) is formed and desorbed from the surface. This process is also known as Eley-Rideal (ER) mechanism; ii) Two absorbed H-atoms on the surface of dust grains are synthesized to molecular hydrogen (H_2), then desorbed. This is known as Langmuir-Hinshelwood (LH) mechanism. These two mechanisms are the extremes, whereas the third one is the intermediate of these two; iii) An absorbed H-atom is bound to the surface and thermalized with the surface. However, the second H-atom does not thermalize with the surface and reacts with the fully thermalized H-atom to form molecular hydrogen (H_2). This is known as the hot atom mechanism (Islam (2010)). The molecular hydrogen in warm molecular gas is observed using higher J rotational states (Goldsmith et al. (2010)), but where the bulk of molecular hydrogen lies is cold molecular gas which does not have energies required for the observation from higher J rotational states.

1.3 Numerical Simulations

Numerical simulations are a vital tool for studying the astrophysical problems of structure formation. Numerical simulations are of crucial importance for theoretical research on galaxy formation. Numerical simulations have played an essential role in the vitality of cosmogony establishment, and they predict the non-linear outcomes of fully specified initial conditions of standard Λ cold matter cosmology. In hydrodynamical cosmology, a range of numerical methods is in use. Lagrangian smoothed particle hydrodynamics (SPH) Lucy (1977), Gingold & Monaghan (1977) and Eulerian mesh-based hydrodynamics (Stone & Norman (1992)) with or without mesh refinement process (AMR) Berger & Colella (1989) and also treating hydrodynamics through an approximation of the collisional Boltzmann equation (Xu (1997), Slyz & Prendergast (1999)) are the most well-known numerical methods. These numerical methods yield conflicting results, though the radiative transfer is not included.

SPH has poor shock resolution and provides low order accuracy for treating contact discontinuities. Moreover, they suppress the fluid instabilities under a few conditions, which results in spurious surface tension. Though it is possible to avoid these effects by introducing heat conduction (Wadsley et al. (2008), Price (2008)) or a modified treatment of the artificial viscosity, it is not confident that it would provide a universal solution. Eulerian methods also lack Galilean invariance, which makes the results insensitive to bulk velocities (Tasker et al. (2008)). This is a severe concern in the simulations of galaxy formation, where the galaxies move with significant speeds (often the order of magnitude greater than the speed of the dense interstellar medium) relative to each other.

A better approach is to let the mesh move. Gnedin et al. (2009a) and Pen (1998) have successfully presented the moving mesh hydrodynamic algorithms (that rely on the Cartesian grids) which are applied for a range of cosmological problems. However, the need to limit maximum grid distortions severely limits the flexibility of the codes when the mesh is heavily distorted. Therefore, an unstructured moving mesh algorithm (mesh defined as Voronoi tessellation of a set of discrete mesh-generating points, which are in principle allowed to move freely) known as AREPO code is proposed by (Springel (2010a)). This code is a moving mesh compromise between SPH and AMR. The use of this AREPO code to produce the model on which this study is carried out is explained in Section 3.

Chapter 2

Literature Review

2.1 Photo - Dominated Region

In the evolution of a galaxy, the interstellar gas is responsible for supplying the power required for star formation in the giant molecular clouds by reserving the materials discharged by the stars (Langer et al. (2010a)). Some Giant molecular clouds slowly convert to stellar nurseries and are identified by the boundaries, which define the transition between the atomic and molecular phases of the interstellar gas. The ionization and heating for these transitions are dominated by far-ultraviolet radiation (FUV). Hence, these boundary regions are known as "Photo-Dissociation Regions" or "Photo-Dominated Regions"(PDR). The photo-dominated regions are formed when far-ultraviolet radiation produced by the young O and B-type stars penetrates through the molecular cloud and dissociates the molecules, which results in the heating of the gas and dust (Escalante (1991)). This makes the Photodissociation region an alliance or sandwiched region in between the ionized region (HII region) (where this FUV is also responsible for the ionization of hydrogen) and the molecular gas region (Bisbas et al. (2021)). Figure 2.1 is a schematic representation of a PDR, where the FUV photons enter the molecular clouds, dissociate the molecules, and form a PDR. In these regions, the H atoms ionizing photons are absorbed into a thin transition zone where the structure changes to almost fully neutral from being fully ionized, and the far-ultraviolet (FUV) photons with energies less than 13.6 eV dissociate the molecular hydrogen and then ionize carbon, which leads to the formation of the HI/CII region. (Tielens (2010)).

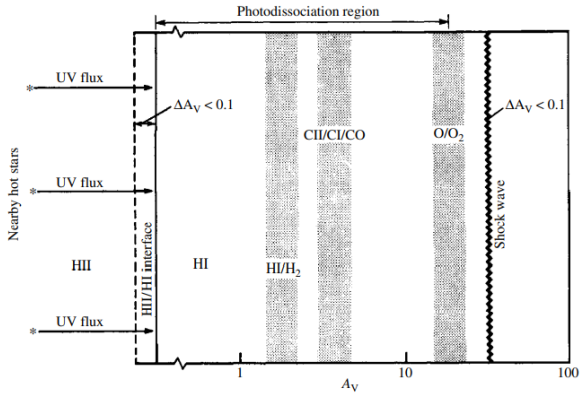

FIGURE 2.1: Schematic view of a photodissociation region. The PDR is illuminated from the left by a strong FUV field (Tielens (2010))

2.1.1 H_2 and CO in interstellar medium

The most abundant molecule in the interstellar medium (Cazaux & Tielens (2004), Hall, Stanimirović, Lee, Wolfire & Goldsmith (Hall et al.), Bolatto et al. (2013), Burgh et al. (2007)) molecular hydrogen (H_2) is a diatomic molecule with identical nuclei, is formed at a temperature of few 10K. As a result of consisting of identical nuclei, H_2 does not possess a permanent dipole moment and dipolar rotational transitions. In the infrared at λ = 28.22 μm and shorter wavelengths, the lower-level energy transitions are purely rotational quadrupole transitions, which are weak. Also, the upper-level energy of the lowest para and ortho hydrogen transitions are at 510K and 1015K above the ground state. Thus, H_2 is excited in gas with temperatures $\geq$ 100K (Dabrowski (1984)), and the excitation of the lowest vibrational transition is difficult. As a result, all these properties of H_2 are concealed in emission in the interstellar (Bolatto et al. (2013)) medium, making it not detected directly in the cold medium. Though $H_2$is the most abundant molecule, the interstellar gas consists of heavier elements like oxygen, carbon, and nitrogen.

CO is the second most abundant molecule in the interstellar medium (den Brok et al. (2021)). Because of its high abundance (though with low excitation temperature), CO is considered to be the common tracer of H_2. H_2 interacts with CO via collisions which provide an advantage for CO line intensities and shapes to be a quantitative measure of H_2 volume density and kinetic gas temperature (Kalberla et al. (2020)). CO has strong ground-state transitions, which produce detectable emission lines at radio wavelengths. The molecular gas mass, which is estimated by the observation of ^{12}CO (J=1-0) spectral line in its lowest energy level corresponds to a wavelength of λ = 2.6 mm (Planck Collaboration et al. (2011a)). This spectral line is optically thick, and, in these limits, the information

that provides molecular gas mass is the line width. The emission line from CO is observed in the units of Kkms^{-1}, which is known as velocity integrated line intensity (W_{CO}). Along with W_{CO} an empirically derived factor generally known as the conversion factor (X_{CO}) with units of cm^{-2}K^{-1}km^{-1}s is multiplied to obtain the molecular hydrogen column density (Shetty et al. (2011);Bolatto et al. (2013)).i.e

$$N_{H_2} = X_{CO} \times W_{CO}\, cm^{-2} \tag{2.1}$$

where N_{H_2} is known as molecular hydrogen column density

As CO is the second most abundant molecule, it is excited at very low temperatures, which is a disadvantage for detecting H_2 in the interstellar medium as H_2 excitation temperatures are very high, i.e., It shields itself from the dust from UV photo-dissociation of CO (Luo et al. (2020)). The far-ultraviolet rays photo dissociates CO and reduces its abundances in the region with intermediate extinctions (($A_v \approx 0.2 - 2$magnitude) see Li et al. (2018)). Moreover, thus, CO photo dissociates, and much of carbon presumably is present in the form of C^+ (Hollenbach et al. (2009); Goldsmith et al. (2008)). This CO property makes it a partial H_2 tracer as some amount of H_2 cannot be traced.

2.2 CO-dark gas

This has been observed in the analysis of the results of Gamma-ray observations from COS-B (Bloemen et al. (1986)) and the Energetic Gamma-Ray Experiment Telescope (Strong & Mattox (1996)) experiments which were conducted to estimate the mass of molecular hydrogen in the interstellar medium. The analysis of these experiments indicated that more hydrogen mass is present in the interstellar gas, which is not seen in either HI or CO emission. Furthermore, the dust column density maps of the Galaxy from DIRBE and maps of the Two Micron All Sky Survey (2MASS) J-K extinction provide evidence of additional gas that is present and is part of interstellar gas, which is presumably in the molecular form, which is not seen by either HI or CO emission (Grenier et al. (2005)).

This molecular hydrogen gas not traced by CO is termed as "dark gas" by Grenier et al. (2005). The ratio of molecular hydrogen mass that is not traced by CO to overall molecular hydrogen mass is defined as the "CO-dark gas fraction" in this thesis. A hypothesis is that nearly 30% of the molecular hydrogen may not be traced by CO, i.e., 30% is dark gas in the molecular clouds (Busch et al. (2019b)). Knowing the great importance of molecular hydrogen in the study of star formation, knowing the amount of hydrogen in the molecular form to

be known completely, is of great importance. Hence, precisely determining or estimating the CO-dark gas fraction in the molecular gas is crucial.

2.3 Aim and Motivation

The theoretical study on CO-dark fraction conducted by Wolfire et al. (2010) on a 1D PDR model estimates that CO-dark gas fraction is a function of mean extinction with characteristics of observed GMC, i.e., as the mean extinction increases the CO-dark gas value decreases and the CO dark-gas fraction is 0.3 with little dependence on CO mass or interstellar radiation field strength. The CO-dark gas fraction has been quantified observationally by many researchers. Grenier et al. (2005) have used large-scale maps of dust emission and extinction γ -ray emission and HI and CO emission with the primary objective of proving that a significant fraction of gas that was traced in dust emission and absorption and in the γ - ray emission but was not seen either in HI emission or CO emission. They quantified the dark gas fraction as 0.33-0.5. In order to interpret the mass of CO-dark gas compared to CO bright gas Planck Collaboration et al. (2011b) have constructed the all-sky map of dust temperature and optical depth along with co-relating them with HI and CO emission. They have estimated that CO-dark gas is 18% times CO-bright gas at high galactic latitudes by mass, and the CO-dark gas fraction value is 0.54. Paradis et al. (2012) have used dust extinction maps instead of Plank far-infrared maps and have estimated the CO-dark gas fraction as 0.62 but considering only at high galactic latitudes and also proclaimed that the CO-dark gas fraction varies for the inner and outer galaxy (the inner galaxy has a CO-dark gas fraction value of 0.71 and the outer galaxy has the value of 0.43). In the molecular phase of the Milky Way, the CO-dark gas component has been calculated to be approximately 30%. Also, it has been interpreted that the CO-dark gas component is not constant but varies with Galactocentric distance (R_G). For R_G = 3 kpc of the Galactic Centre, the CO-dark gas fraction is essentially zero, but for R_G = 10 kpc, the value of the CO-dark gas fraction is in the range of 0.6-0.8. This has been achieved by Pineda et al. (2013) by studying the [CII] emission by using the GOT C+ (Galactic Observations of Terahertz C^+) survey Langer et al. (2010b) and determining the excess emission which is not deduced by either HI or CO emissions produced by co-relating the [CII] emission with HI and CO emission. In terms of numerical simulations, modeling groups like Dobbs et al. (2008a); Gnedin et al. (2009b); Christensen et al. (2012) have modeled a large-scale dynamical simulation of the interstellar medium. Nevertheless, such models only consist of resolutions that allow one to study giant

molecular clouds(GMCs) individually. Moreover, small, scale resolution models produced by groups like Glover et al. (2010); Glover & Clark (2012a) do not consist of sufficient dynamical range for the formation of cloud self-consistently. By using a three-dimensional PDR code 3D-PDR (Bisbas et al. (2012)) Offner et al. (2013) have estimated the CO-dark component to be found in the temperature range of 30K-70K.

As we know the importance of H_2 in understanding the star formation region and evolution of the interstellar medium, it is vital to know the total budget of H_2 in the interstellar medium. Since the H_2 cannot be entirely detected by CO as a tracer, estimating the CO-dark gas fraction is of more importance. All the above-stated previous works to determine the CO-dark gas fraction are based on the different interstellar medium conditions but not on the resolution quality. All the above factors motivate this thesis to be focused on the behavior of CO-dark gas fraction in the fiducial Milky Way simulation (with the considerations of large-scale galactic effects supernova feedbacks and differential rotations) on different sizes of the AREPO cells.

This thesis aims to investigate the CO-dark gas fraction and determine the CO-H_2 conversion factor X_{CO} at different spatial resolutions for the $10M_{\odot}$ resolution region and its subregions of the potential dominated region from the fiducial Milky Way simulation. Furthermore, to evaluate whether the CO-dark gas fraction can be determined on our knowledge of N_{H_2}, N_{HI} and N_{SD}.

The structure of this thesis is like this: In chapter 3, I have described the model of the fiducial Milky Way, using which this thesis carried out. Then, in chapter 4, I have explained in detail the methods used to determine the column densities of CO (N_{CO}), H_2 ($N_{H_2}0$, HI (N_{HI}), total (N_{SD}) and also the CO-dark gas fraction and the methods used to compare the behavior of CO-dark gas fraction on different aperture sizes. In chapter 5, I have discussed the results obtained from the methods used to achieve the aim of this thesis and have discussed the sources of uncertainties and caveats. Then, in chapter 6, I have compared the results obtained in this thesis with theoretical and observational works. Finally, I have concluded my thesis in chapter 7.

Chapter 3

Model

A model of the interstellar medium is necessary to compute the CO-dark gas fraction. An ideal model for this purpose will comprise the dynamical evolution of the interstellar medium and the chemical evolution (like heating, cooling, and ionization states which are the significant factors that modify the properties of the interstellar medium) in a self-consistent fashion. The evolution of the interstellar medium is indicated in high dynamical range 3D simulation by including the H_2 and CO chemistry. Few research groups have produced the models by 3D simulations of an interstellar medium with different criteria. Some research groups like Dobbs et al. (2008b); Gnedin et al. (2009b) ; Christensen et al. (2012) have developed large-scale dynamical simulation which accounts for the H_2 formation (CO chemistry is not included), but it is not consistent for the study of individual giant molecular cloud as it does not provide the resolution required for it. Small scale models are produced by Glover et al. (2010); Glover & Clark (2012a) represents the formation of H_2 and CO in the turbulent interstellar medium but lacks the dynamical range required to model the clouds self-consistently. Hence, combining large-scale dynamical 3D simulations, small-scale gas cooling physics, and chemistry of the interstellar medium is required. Smith et al. (2020) have produced such models (Potential dominated and clustered supernova feedback).

This model is generated using a modified version of AREPO code (Springel (2010b) ;Pakmor et al. (2016)) which includes the custom interstellar medium physics modules. AREPO is a well-tested cosmological code that uses Voronoi mesh to solve the (M)HD equations by combining the strengths of grid-based Eulerian hydrodynamical codes and smoothed particle hydrodynamics (SPH). AREPO mesh is adaptive, and thus it can provide high-resolution mass refinement at the places of interest. This high-resolution mass refinement feature of

AREPO helps address the challenges involving extreme dynamic range and discontinuous and fluid instabilities without specific geometry. Furthermore, the performance of AREPO is better than standard SPH for modeling the subsonic turbulence (Bauer & Springel (2012)) and highly multiphase flows (Sijacki et al. (2012)). These properties of AREPO make it an ideal tool for observing the complexes like star formation in galaxies with an extensive dynamic range. The initial conditions, properties, and the environment in which the simulation is performed is discussed in the following sections.

3.1 Galactic Potential

The author's primary objective of Smith et al. (2020) is to produce the simulation of a spiral galaxy and study the behavior of interstellar medium present in that galaxy with large-scale galactic effects. Therefore, it was chosen to systematically model the large-scale galactic potential to minimize the computational effort. A logarithmic potential (produces a flat rotation curve of $v_0 = 220 kms^{-1}$) (Binney & Tremaine (1987)) and the potential for the outer halo from Caldwell & Ostriker (1981) are combined, and the spiral perturbations are also included to the potential of the model, which is a four-armed component upon a disc of gas without self-gravity with pitch angle $\alpha = 15^{\circ}$ and a pattern speed of 2×10^{-8} rad yr^{-1} adapted from Cox & Gómez (2002). Using the Arepo gravitational tree (Springel (2010b)), the self-gravity of the gas is calculated. The most significant fitting potential from McMillan (2017a) has been used for the axisymmetric part of gravitational potential, which is generated to be accordant with the various theoretical and observational constraints for the Milky Way. It is an addition of the halo, bulge, and disc component (For the detailed description, see Smith et al. (2020); Smith et al. (2014)).

3.2 Gas Chemistry

The formation of hydrogen molecule (H_2) on grains and destruction by photodissociation, cosmic-ray ionization, and collisional dissociation of atomic hydrogen and recombination on grain surfaces and in the gas phase of H^+ is included for hydrogen gas chemistry along with using the hydrogen gas chemistry of Glover & Mac Low (2007a) and Glover & Mac Low (2007b). Nelson & Langer (1997) is a simplified chemical model that assumes the direct conversion of C^+ to CO or vice-versa without taking into account of the intermediate reactions (like the formation of C). It is assumed that the conversion of C^+ to CO is initiated by the

formation of an intermediate hydrocarbon radical by the radiative association reaction $C^+ + H_2 \rightarrow CH_2^+ +$ photon with a reaction rate coefficient k_0. This ion molecule rapidly converts to carbon radicals (CH or CH_2) via ion-molecule reactions H_2 and dissociative recombination with electrons. These radicals either react with atomic oxygen to form CO with a reaction rate coefficient (k_1) or undergo photo-dissociation. Once CO is formed, C and O are yielded by CO only via photo-dissociation, and the formed C is converted to C^+ immediately by instant photoionization. The equation that they have provided, which describes the rate of production or destruction, is:

$$\frac{dn(CO)}{dt} = k_0 n_{C^+} n_{H_2} \beta - \Gamma_{CO} n_{CO} \tag{3.1}$$

where n_{C^+} is the number density of C^+ ions and n_{H_2} is the number density of hydrogen molecules. $k_0 = 5 \times 10^{-16}$ cm^3 s^{-1} and Γ_{CO} is CO photodissociation rate (10^{-10} G_0 exp(-2.5 A_V) s^{-1})(Nelson & Langer (1997)). Using this model is the same as the NL97 model from Glover & Clark (2012c), and it also describes the complete details of the combined network and terms of speed and accuracy.

The incident far-ultraviolet radiation field and density govern the structure of PDR. These are expressed in terms of interstellar radiation field (Tielens (2010)). The interstellar radiation field (ISRF) is assumed to have the same spectral shape and strength as the solar neighborhood, which is derived by Draine (1978) and it is equivalent to 1.7 times field strength derived by Habing (1968). TreeCol algorithm developed by Clark et al. (2012) is used to treat the attenuation of ISRF caused by H_2 self-shielding, CO self-shielding, the shielding of CO by H_2, and by also dust absorption. The 4π steradian map of dust extinction, CO, and H_2 column densities surrounding each AREPO cell are carried out using this TreeCol algorithm. For simulations of large-scale galactic potential, using the TreeCol algorithm overestimates the column densities. Thus, to prevent the overestimation of column densities, a shielding length (L_{sh}) of 30pc (which approximately corresponds to the nearest O or B star in the solar neighborhood (Reed (2000)) is defined such that the contributions of the gas at length $L \leq L_{sh}$ from each AREPO cell is only considered. This field does not explicitly include ionizing radiation from massive stars. It only represents the general background radiation field.

3.3 Gas Cooling

The cooling function of atomic and molecular gas from radiative processes is described in Clark et al. (2019). Using H and e^- abundances directly from the non-equilibrium chemical model, modeling the cooling function of high-temperature gas ($T > 10^4$K) via atomic hydrogen line emission is achieved. Assuming that helium and metals are in collisional ionization equilibrium using values from Gnat & Ferland (2012) high-temperature cooling for helium and metals are computed. Cosmic ray ionization rate is taken as 3×10^{-17}s for atomic hydrogen and molecular hydrogen twice this value. Metal abundance is assumed to be the same as solar metal abundance, and the gas-to-dust ratio is 100:1.

3.4 Supernova feedback

The stellar feedback in the interstellar medium includes stellar winds, jets, photoionization regions, and supernovae feedback. The authors of Smith et al. (2020) have considered only supernovae feedback due to high complexity at galactic scale simulation, including all the effects (which is a caveat of their work). Supernovae feedback injects both momentum and thermal energy into the neighboring gas. They have adopted two types of supernovae feedback, i) purely random supernovae explosions and ii) supernovae tied to sinks. This thesis is carried out on the model, which is produced by considering purely random supernovae explosions. It is assumed as one supernova explosion per 50 years, which is typical for the Milky Way, and the sample points are randomly chosen from the initial gas density profile for the disk.

3.5 Simulations

Inspired by the Milky Way gas disc model from McMillan (2017b) (which consists of two density distributions for HI and H_2 at large radii it exponentially declines), the simulations for this model are started by setting up of a gas disc. Both conditions are included as the initial condition for the simulation, and the simulation starts from an atomic state. The main study is based on the molecular gas, forming from the atomic gas phase as the disc evolves.
The gas distribution is let to respond to the large-scale potential for the first 150 Myr, and spiral arms are developed with purely random feedback without the self-gravity of the gas. For the mass refinement process, 1000 $M_\odot$ is defined as

the target mass in each AREPO cell for the efficiency of the simulations. The middle phase for 70 Myr begins after 150 Myr, where a high-resolution box is created between two spiral arms within 3kpc that co-rotates with gas when the steady state is achieved after 150 Myr. The formation timescale of H_2 in the interstellar medium is approximately, $\frac{10^9 \mathrm{yr}}{\mathrm{n}}$ where 'n' is the number density (cm^{-3}) Hollenback & McCray (1975). The characteristic mean number density for most giant molecular clouds is 100 cm^{-3}, which shows that the approximate H_2 formation time in a giant molecular cloud is 10Myr Blitz & Shu (1980). Thus, for the middle phase, the gas mass resolution target is initially set to 100 $M_\odot$ once the middle phase crosses 60 Myr. The target mass resolution is set to 10 $M_\odot$ for the last 10Myr as it resembles the surface density value of the Milky Way (hereafter, this region is mentioned as 10$M_\odot$ resolution region). In this gas phase, self-gravity is turned on, and sink particles are formed. Since the supernova feedback is purely random, the gas dynamics in this model can be determined by the gravitational potential of large scales. As the random feedback is not efficient for moving around the dense gas, the dynamics are dominated by the gravitational potential of large scales, which leads to the clear, sharp spiral arm. Figure 3.1 represents the overall view of the potential dominated model produced by Smith et al. (2020). The color bar represents the surface density of the model.

This thesis is accomplished on the black square box region shown in Figure 3.1. This region is the 10$M_\odot$ resolution region, which is obtained by the mass refinement process at the mid-phase of the simulation.

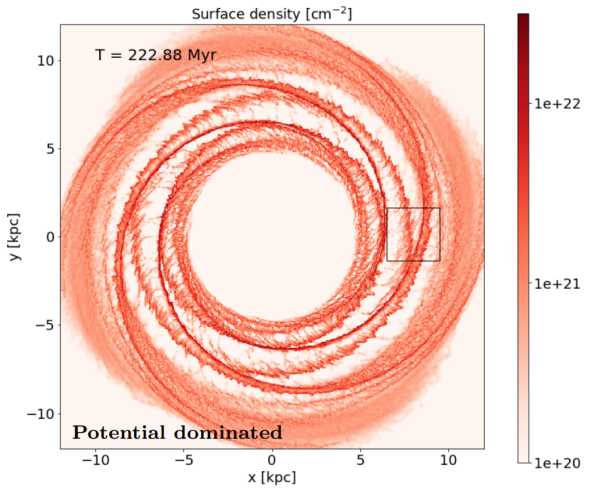

FIGURE 3.1: Simulation of the potential dominated model. The black square box indicates the region of 10 $M_\odot$ resolution (image credit: Smith et al. (2014)).

Chapter 4

Methodology

4.1 Data

The overall specifications and the properties of the potential dominated model in which a particular region is considered, and this thesis is performed, are discussed in section3. Smith et al. (2020) work aims to study the molecular gas in molecular clouds in the form of filaments. Furthermore, these filaments are formed away from the disc, and this region in the potential-dominated model is produced by Smith et al. (2020) and Smith et al. (2014) with the mass refinement of each AREPO cell with the target mass of 10 $M_{\odot}$. This is the ground on which the 10 $M_{\odot}$ resolution region is considered for this thesis. The dimensions of the AREPO cell for this region are 3kpc and are shown in Figure 4.1. The letters A and B in Figure 4.1 represent the location of cloud complexes in the potential dominated region, on which Smith et al. (2020) group has studied the impact of the galactic-scale forces on the filament network formed in these and the other two cloud complexes (Supernova feedback region in their paper). The AREPO simulation data of this 10 $M_{\odot}$ resolution region is provided by Rowan.J.Smith, and the coding part of this thesis is performed using arepy packages and other basic packages (available to the public) in Python-Jupyter Notebook. The overall 3D 10 $M_{\odot}$ resolution region is divided into nine equal-sized boxes of size 1kpc (hereafter, it is mentioned as subregion/subregions). Each subregion is of a size of 400 pixels along each axis.

4.2 Method

As the initial step of the thesis, given 3D model data is converted to 2D (enables comparison with the observational data), which is achieved by projecting

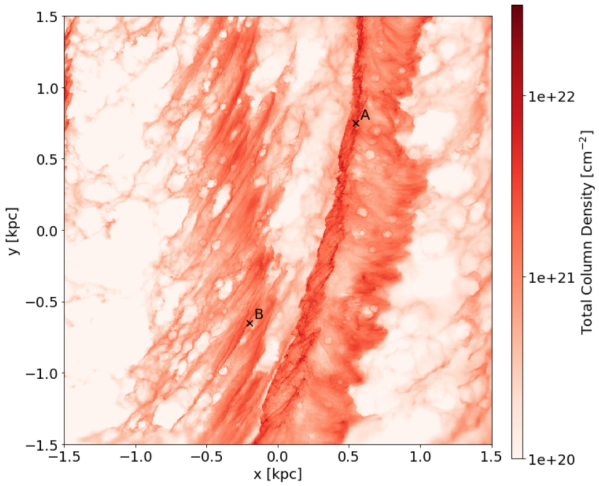

FIGURE 4.1: Zoom image of 10 $M_\odot$ resolution regions of potential dominated model (image credit:Smith et al. (2020)).

the 3D data onto the grid along the line of sight (z-axis). Then, equation 4.1 is used to calculate the molecule's mass or the element of which the 2D data is determined. For example, if the mass of CO is required, then the number density of CO molecules and CO molecular weight is used, and the mass of CO is determined. Once the mass of the required form of gas is achieved, the column density of the required gas is obtained using equation 4.2 where x denotes the particular molecule or element, and density-weighted temperature is calculated. By using this procedure, the quantities Total Column density (N_{SD}), H_2 column density (N_{H_2}), CO column density (N_{CO}) and atomic hydrogen (HI) column density (N_{HI}) are determined.

$$M_{x_i} = n\ V_p\ \mu\ mp\ (grams) \tag{4.1}$$

where x is the element or the molecule, 'i' is the number of AREPO pixel, 'n' is the number density [cm^{-3}] (which is derived from the AREPO density grids by multiplying with internal AREPO density units and diving by mp), 'μ' is the weight of the corresponding molecule, 'V_p' is the pixel volume of the image, 'A_p' is the pixel area of the image [cm^{-2}], 'mp' is mass of a proton (1.6726231×10^{24} grams)

$$N_{x_i} = \frac{\sum_{i=1}^{i=400} n\ x_n\ V_p}{A_p}\ cm^{-2} \tag{4.2}$$

where x_n is the fractional abundance of the molecule.

Figures 4.2,4.3, 4.4 and 4.5 and represents the AREPO images of N_{SD}, N_{CO}, N_{H_2} and N_{HI} for all the subregions respectively. From Figures 4.3 and 4.4 it can be observed that there are some regions with no CO at but H_2 is present. This

indicates the presence of CO-dark gas.

From Table 1.1, it can be noted that as the gas temperature increases, the density of the interstellar gas decreases and vice-versa. The interstellar gas at low temperatures will be in the molecular phase, at high temperatures in the ionized state, and at intermediate temperatures in the neutral phase. Figure 4.6 represents the mass-weighted 2D histogram, i.e., the Log of number density(n, in the unit cm^{-3}) against the Log of temperature (T, in K) of the subregions, which helps in understanding the chemical state of the gas, and it is observed that at the temperatures of range 10K to 10^2 K the interstellar gas is dense, and the gas is molecular.

Fractional molecular hydrogen abundance is calculated using the expression $f_{H_2} = \frac{2N_{H_2}}{2N_{H_2}+N_{HI}}$. Figure 4.7 presents the plot of f_{H_2} as a function of N_{sd}. It is observed that 50pc and 100pc spatial resolutions show the fractional molecular hydrogen abundance relative to total hydrogen to be little less than 250pc and 500pc spatial resolutions at column densities 10^{18} - 10^{19} cm^{-2}. However, at column densities between 10^{20} and 10^{21} cm^{-2} the fractional H_2 abundance increases dramatically as H_2 self shielding begins and the fractional H_2 abundance is constant for column densities between 10^{21} and 10^{22} cm^{-2}. Such dramatical rise in H_2 fractional abundance is also observed in Leroy et al. (2007) and Wolfire et al. (2008). This trend of f_{H_2} is in good agreement with Gnedin et al. (2009a) where a galactic scale model of molecular hydrogen formation is presented. These observations were used to calibrate a clumping factor, accounted for small-scale, unresolved resolved density fluctuations, and tuned to ensure that the model matched observations. However, N_{SD} is lower for a given value of f_{H_2} than observational data (e.g., Savage et al. (1977)) whose observations were considered along long sight-lines within the galactic disc which consists of high column densities than in face on the disc which is used in my observations.

Figure 4.8 shows the 2D histogram of N_{CO} and N_{H_2} for the 10 $M_\odot$ resolution region which in good agreement with Figure 6 of Smith et al. (2014) where it is specified that at $N_{H_2} > 10^{21}$ cm^{-2} the simulation produces slightly more CO than by the observations of Sheffer et al. (2008). The large difference between their simulations and the observations are observed at $N_{CO} < 10^{15}$ cm^{-2}. As the gas at low column densities do not produce much of CO emission, the produced CO column densities do not affect the results. To compare the simulation outputs with the observational data, the CO abundance relative to H_2 is determined. The column-averaged CO abundance relative to H_2 is denoted by Z_{CO} and defined as $\frac{N_{CO}}{N_{H_2}}$. As the initial conditions for the fiducial Milky Way simulations, the maximum CO abundance is assumed and defined as 1.4×10^{-4}. Figure 4.9 shows the

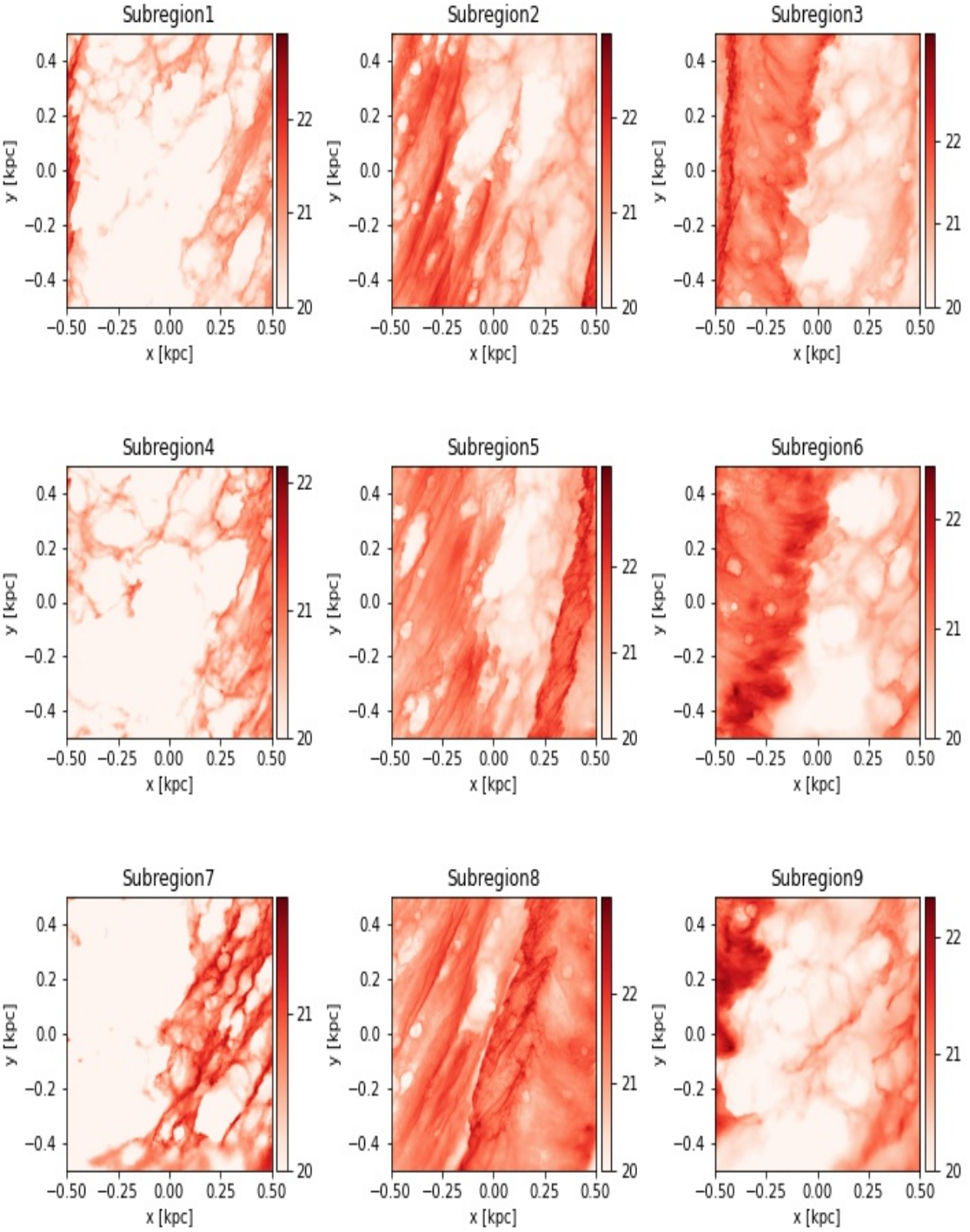

FIGURE 4.2: AREPO image showing the color scale of $\log_{10}(N_{SD}[cm^{-2}])$ for all 9 subregions.

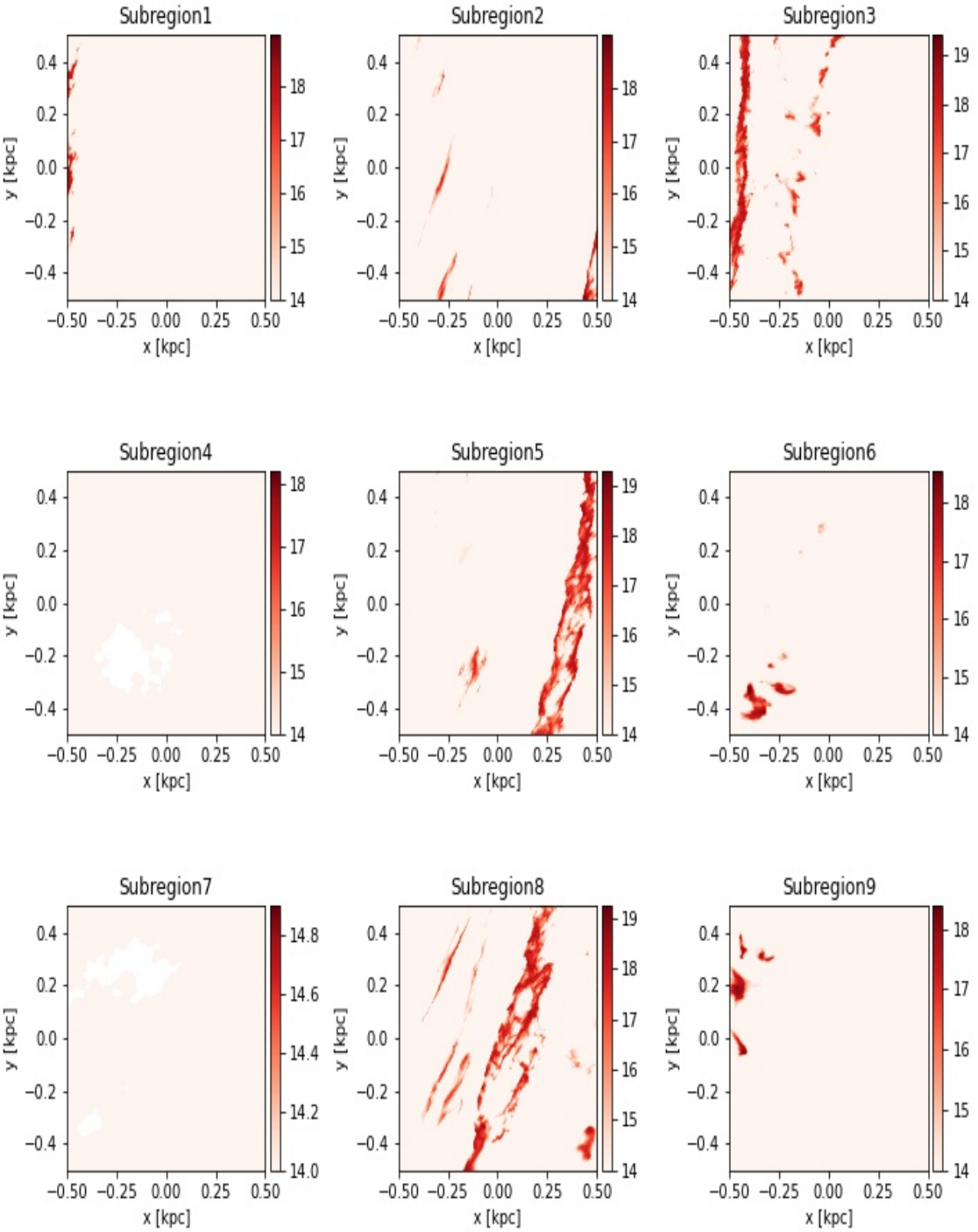

FIGURE 4.3: AREPO images showing the color scale of $\log_{10}(N_{CO}[cm^{-2}])$ for each subregion.

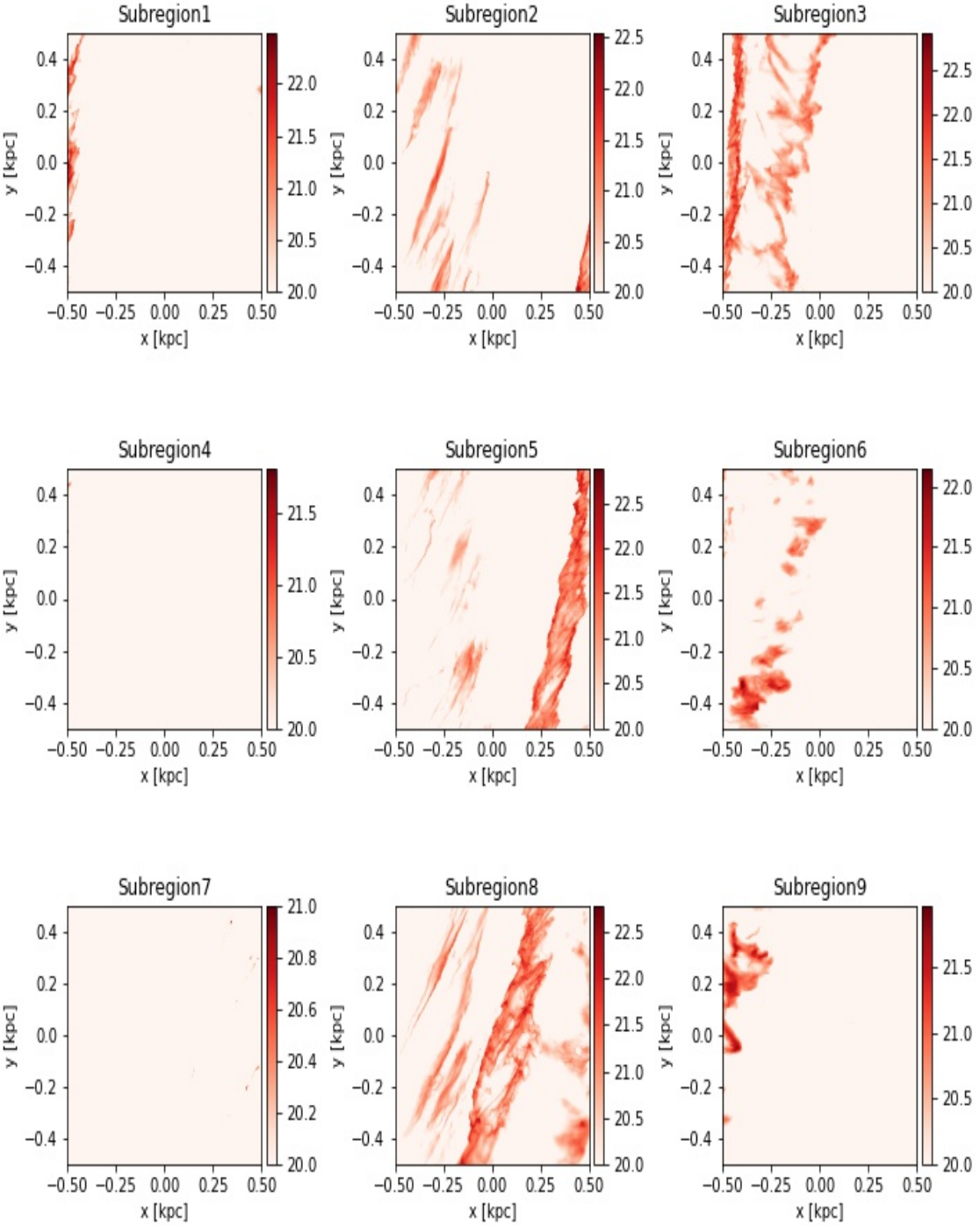

FIGURE 4.4: AREPO image showing the color scale of $\log_{10}(N_{H_2}[cm^{-2}])$ for each subregion.

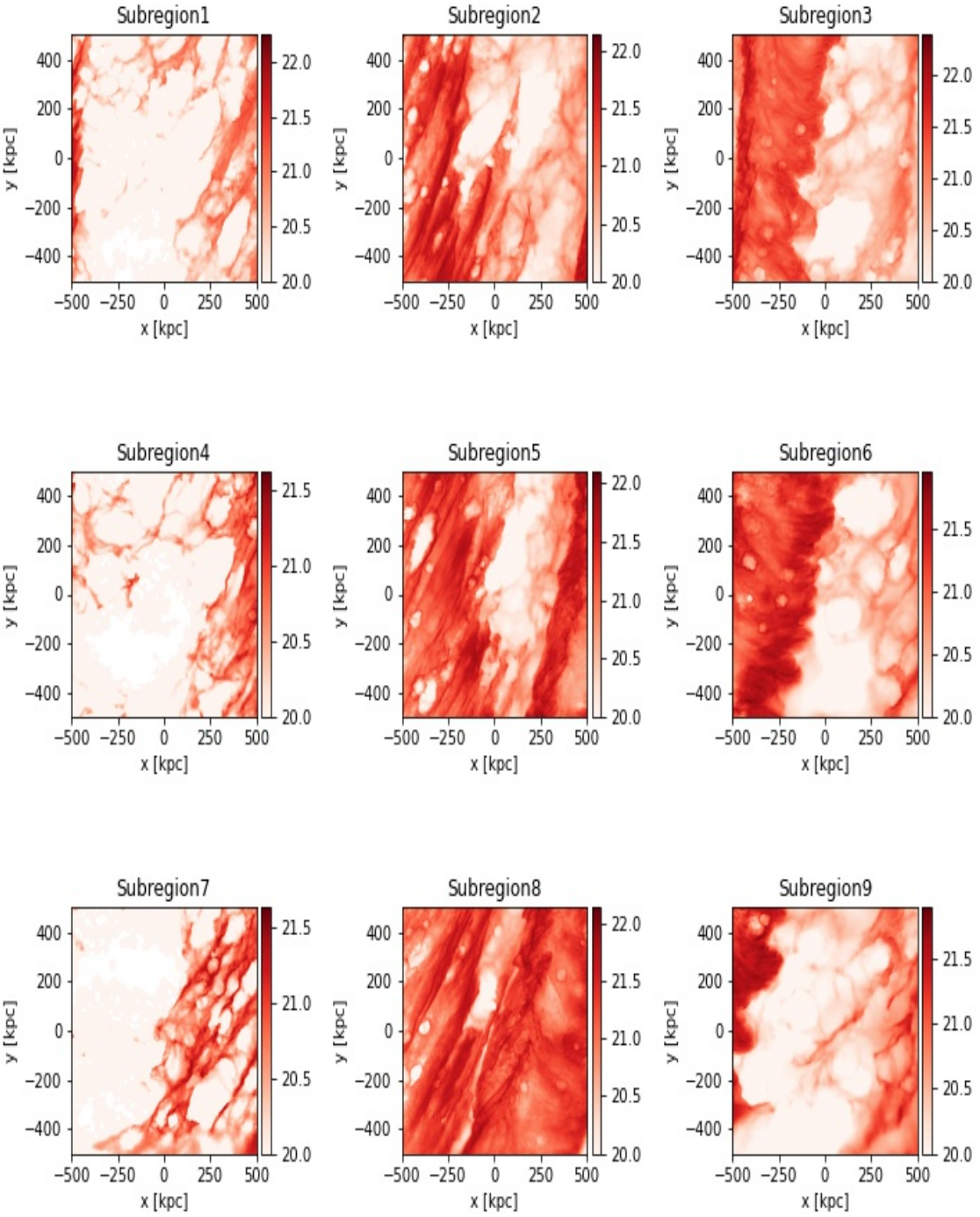

FIGURE 4.5: AREPO images showing the color scale of $\log_{10}(N_{HI}\ [cm^{-2}])$ of each subregion.

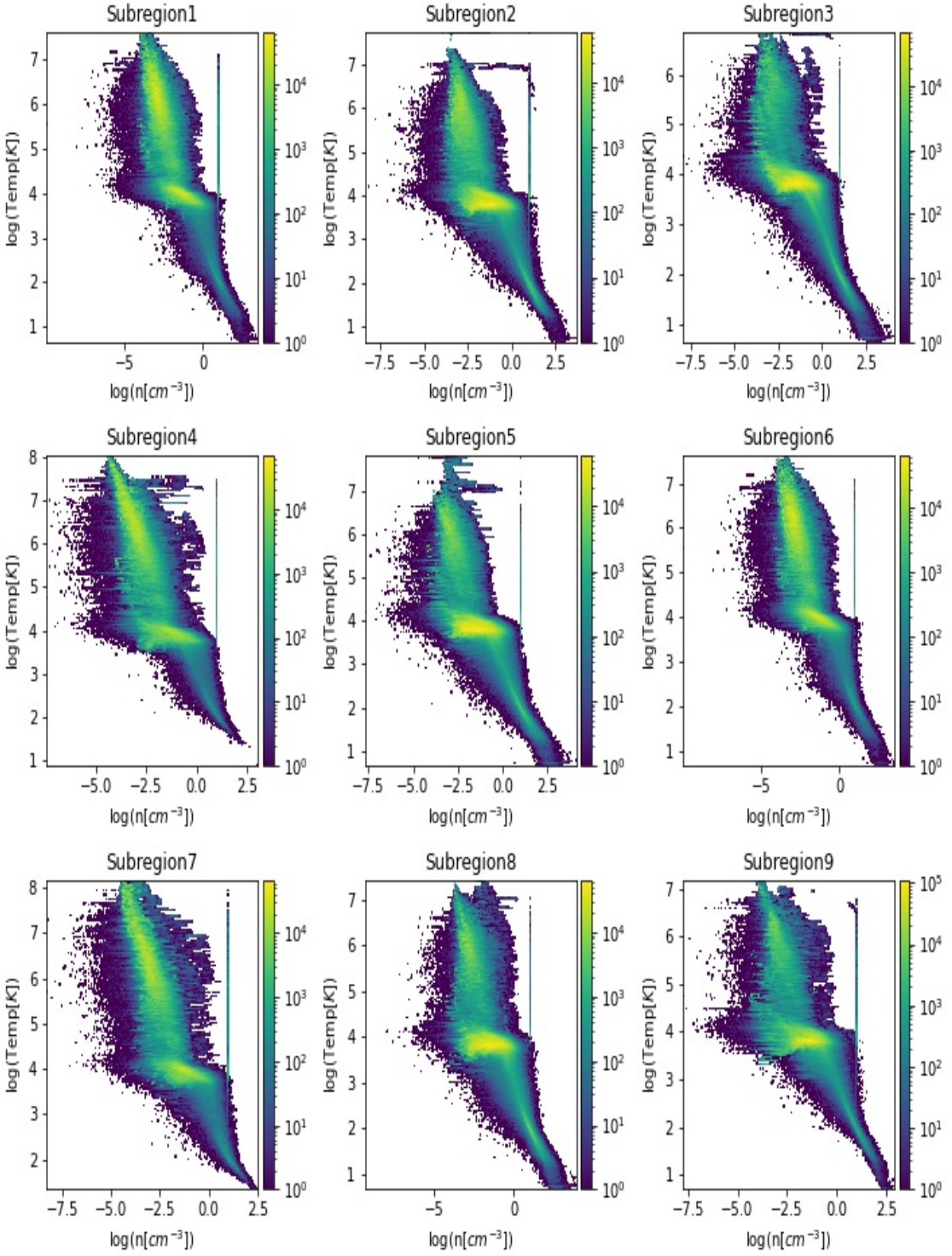

FIGURE 4.6: The phase plot of 9 divided subregions where each image corresponds to the actual region in their exact location. The colorbar represents the counts per bin

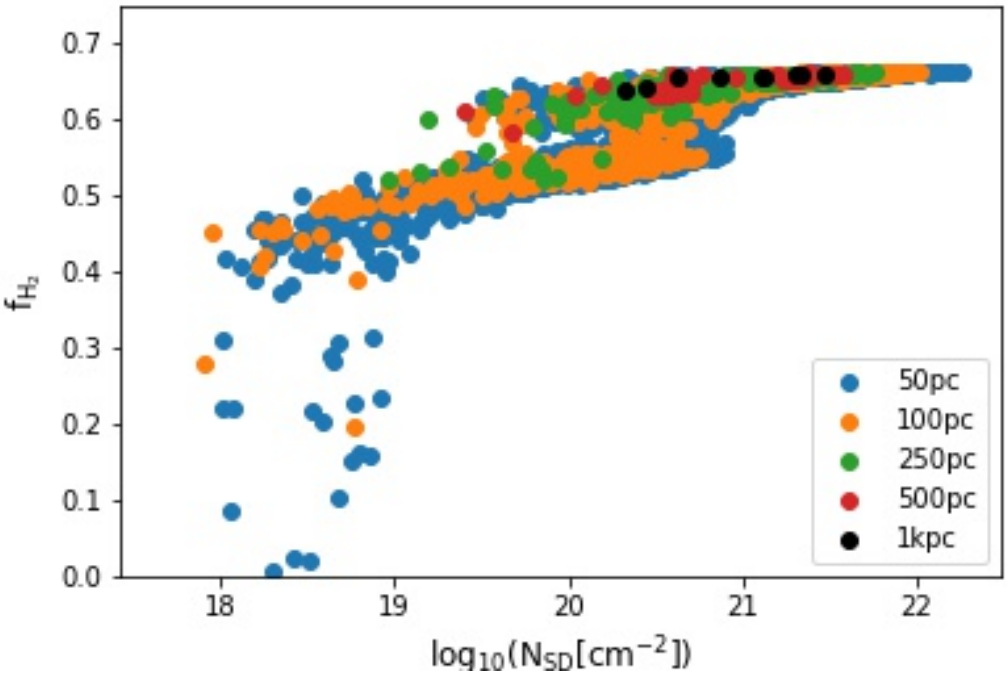

FIGURE 4.7: Fractional H_2 abundance relative to total hydrogen as a function of the column density of all spatial resolutions.

2D histogram of the relation of Z_{CO} and N_{H_2} (The characteristic N_{H_2} for CO-dark regions are in the range of $10^{20} < N_{H_2} < 10^{21}$ cm^{-2} (see Figure 6 in Smith et al. (2014)). Thus, the N_{H_2} is set to the lower limit of 10^{18} cm^{-2} in the image to study the relation in detail in both Figures 4.8 and 4.9). At $N_{H_2} > 10^{21}$ cm^{-2} there is slightly high CO produced than estimated by Sheffer et al. (2008) (some upper limits are included here also) from their UV absorption (note: even some upper limits are included). This is due to the use of Nelson & Langer (1997) chemical network, which overproduces CO in dense clouds Glover & Clark (2012b). At lower column densities, an increasingly large discrepancy developed between the observed and simulated CO column densities. Many authors have discussed the difficulties present in deriving the observed N_{CO} - N_{H_2} relation at low N_{H_2} with standard PDR models. However, a large difference between the results presented in this thesis and Sheffer et al. (2008) observations are only for $N_{CO} < 10^{15}$ cm^{-2}. In Figure 4.9 it is seen that where the molecular gas tends to be dark (i.e., at $N_{H_2} < 10^{21}$ cm^{-2}) Z_{CO} is very much lower than 1.4×10^{-4} which is generally assumed value for GMC. There is scatter seen in the distribution of Z_{CO} at $N_{H_2} > 10^{20}$ cm^{-2}, shows that there is considerable variability in column density regime. Such similar variations in Z_{CO} is also observed in diffused gas clouds by Liszt & Pety (2012).

To determine CO-dark gas, a sense of where the bulk of CO emission is produced is to be known. Choosing the simplified curve of growth approach (Pineda et al. (2008),Glover & Mac Low (2011)) the regions of bulk CO emission are determined. This curve growth method is not fully radio-transferred. However, it helps to estimate velocity-integrated intensity (W_{CO}) Kkm^{-1} in the J=1→0 line of CO, which is estimated using equation 4.3.

$$W_{CO} = 2T_{CO}\Delta v \int_0^{\tau_{10}} \beta(\tau)\, d\tau \ (\mathrm{K\ kms^{-1}}) \tag{4.3}$$

where T_{CO} is the CO temperature [K], τ is the optical depth in the observed CO line and $\beta(\tau)$ is the photon escape probability. T_{CO} is defined by the equation 4.4 where $A_{CO,i}$ is the fractional abundance of CO and T_i is the temperature in i cell —assuming that CO is in local thermodynamic equilibrium (LTE) the excitation temperature (T_{ex}) of CO is equivalent to CO abundance temperature (T_{CO}). The high column density sight lines in this study are primarily probe regions with high gas densities and high optical depths in the CO lines and hence the assumption of T_{ex} = T_{CO} is reasonable. However, $T_{CO} \leq$ 100K is only considered because Smith et al. (2014) as shown that CO becomes optically thick at a temperature of few 10K. The optical depth in the CO J=1→0 line is determined by using the equation 4.5.

$$T_{CO} = \frac{\sum_{i=1}^{i=400} T_i A_{CO,i}}{\sum_{i=1}^{i=400} A_{CO,i}} \tag{4.4}$$

$$\tau_{10} = \frac{A_{10}c^3}{8\pi v_{10}^3}\frac{g_1}{g_0} f_0 \left[1 - \exp\left(\frac{-E_{10}}{kT_{ex}}\right)\right] \frac{N_{CO}}{\Delta v} \tag{4.5}$$

where A_{10} is the spontaneous radiative transition rate for the J =1→0 transition, ν_{10} is the frequency of the transition, E_{10} = hν_{10} is the corresponding energy, g_0 and g_1 are the statistical weights of the J = 0 and J = 1 levels, respectively, and f_0 is the fractional level population of the J = 0 level. A_{10} and v_{10} values are taken from Lieden Atomic and Molecular Database (Schöier et al. (2005)). The assumption of CO in LTE provides the value of f_0, which is inversely proportional to the partition function of the CO molecule (Z(T)). The velocity dispersion (Δv) of the gas is estimated by virial theorem and following the arguments provided by Bolatto et al. (2013). The observations of CO bright clouds show that the velocity distributions of the gas in these clouds have velocity dispersions close enough to the velocity dispersions that would have in virial equilibrium. However, it is not necessary that one can conclude that the clouds are in virial equilibrium (Ballesteros-Paredes (2006)). Nevertheless, the clouds that are produced by the

simulations are not in equilibrium. However, the virial theorem supports estimating the velocity dispersion in the simulated clouds by the expression,$\Delta v = \sqrt{\frac{GM}{r_{pix}}}$ where r_{pix} is the radius of the AREPO pixel.

$\beta(\tau)$ is approximated by the assumption that it is the same as for a plane parallel uniform slab (Tielens & Hollenbach (1985).)

$$\beta(\tau) = \begin{cases} [1 - \exp(-2.34\tau)]/4\tau & \text{if} \tau \leq 7 \\ \left(4\tau\sqrt{\ln(\frac{\tau}{\sqrt{\pi}})}\right)^{-1} & \text{if} \tau > 7 \end{cases}$$

Once W_{CO} is determined, CO dark gas fraction can be estimated by distinguishing between CO bright and CO dark gas, which is not immediately obvious how to perform (i.e., from a gas cloud how much faint the CO emission should be to term it as CO dark). Instead of adopting an arbitrary threshold value to distinguish between CO dark and CO bright gas, the CO-dark gas fraction is derived as a function of the choice of threshold. CO dark gas fraction is defined by the equation 4.6 and represented as f_{dg}. With the exact definition for f_{dg} Smith et al. (2014) have clearly shown that 42% of the total molecular mass is present where $W_{CO} < 0.1$ K Kms^{-1} (i.e., little or no CO emission) and 55% of the total molecular mass in their simulation is present where $W_{CO} > 10$ K Kms^{-1}. Moreover, thus only a few percent of total molecular gas is present in this intermediate range, and the threshold can be taken in this range. Using this threshold definition of CO dark and CO bright gas, I have considered $W_{CO} < 10$ K Kms^{-1} as the threshold to differentiate CO-dark and CO-bright gas. Figure 5.3 shows that the derived value of f_{dg} is not particularly sensitive to the threshold taken (black line representing 1kpc spatial resolution)

$$f_{dg} = \frac{M^{x}_{H_2}}{M^{x}_{H_2} + M^{CO}_{H_2}} \tag{4.6}$$

where $M^{x}_{H_2}$ is the mass of H_2 in the pixels below an intensity of x = W_{CO} and $M^{CO}_{H_2}$ is the mass H_2 where CO is bright ($W_{CO} > W_{CO,th}$).

Once all the quantities are determined for $10M_{\odot}$ resolution region and subregions at 1kpc resolution, the spatial resolutions are increased. The quantities and CO-dark gas fraction are determined, and their behavior is studied. I have increased the spatial resolution of the AREPO image from 1kpc to 50pc of the subregion in regular intervals to study if the CO-dark gas fraction is sensitive to the spatial resolution of the AREPO image that is studied. The spatial resolutions of the AREPO image considered for this work are 500pc, 250pc,100pc, and 50pc. This is achieved by dividing the 1kpc subregion (consisting of 400 AREPO cells in each) into four parts consisting equal number of AREPO cells in each

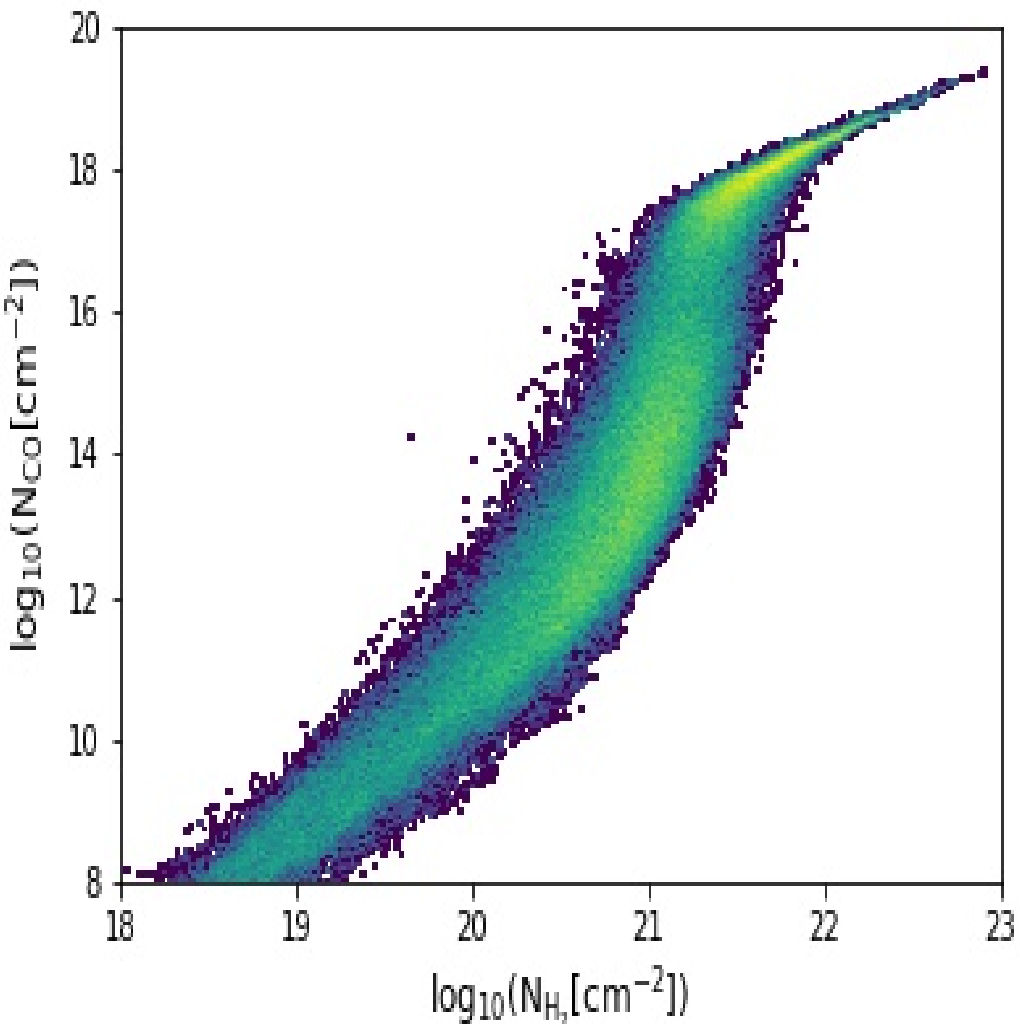

FIGURE 4.8: Relation between N_{CO} and N_{H_2} for $10M_{\odot}$ resolution regions. The plotted points are the 2D histogram of the gas distribution, with green color represents the densely populated and dark blue representing the least populated part of the distribution.

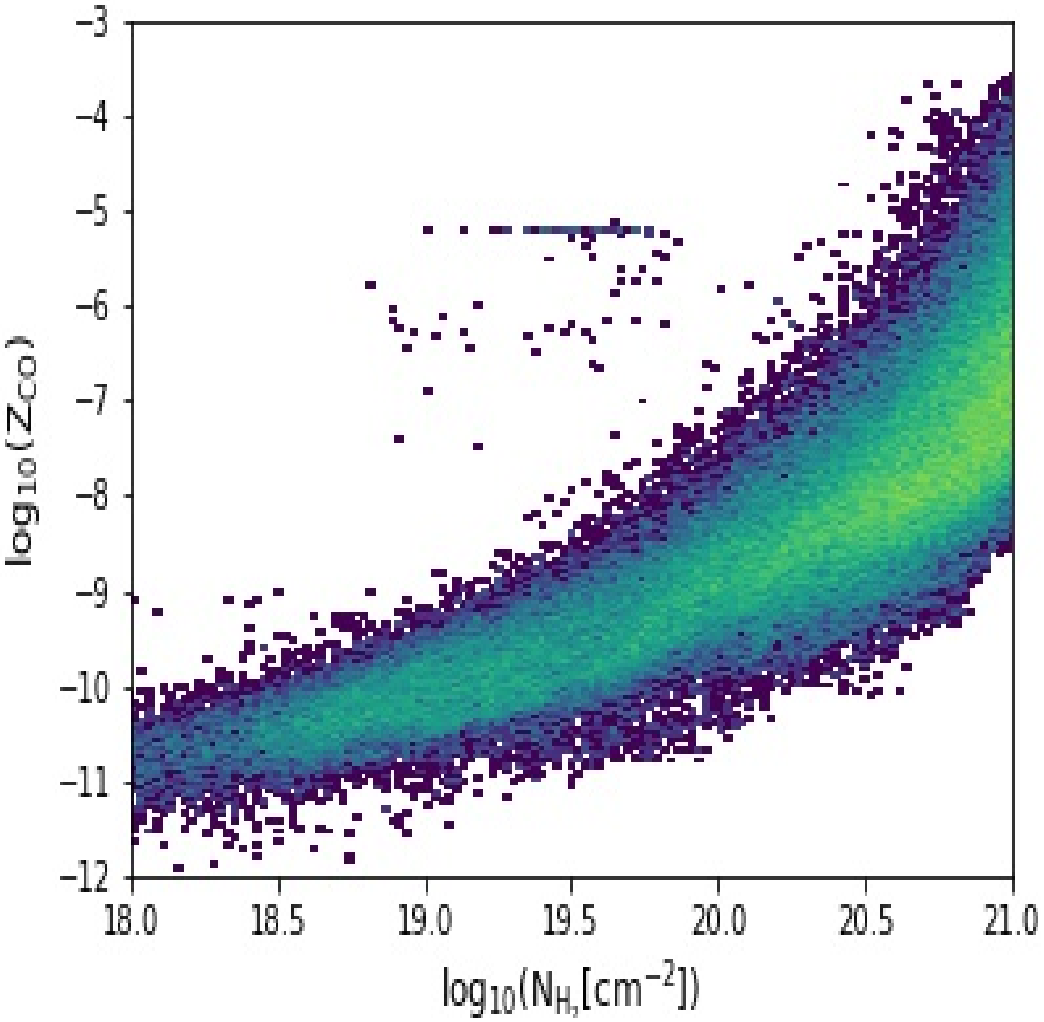

FIGURE 4.9: Relation between Z_{CO} and N_{H_2} $10M_{\odot}$ resolution regions. The plotted points are the 2D histogram of the gas distribution, with green color represents the densely populated and dark blue representing the least populated part of the distribution.

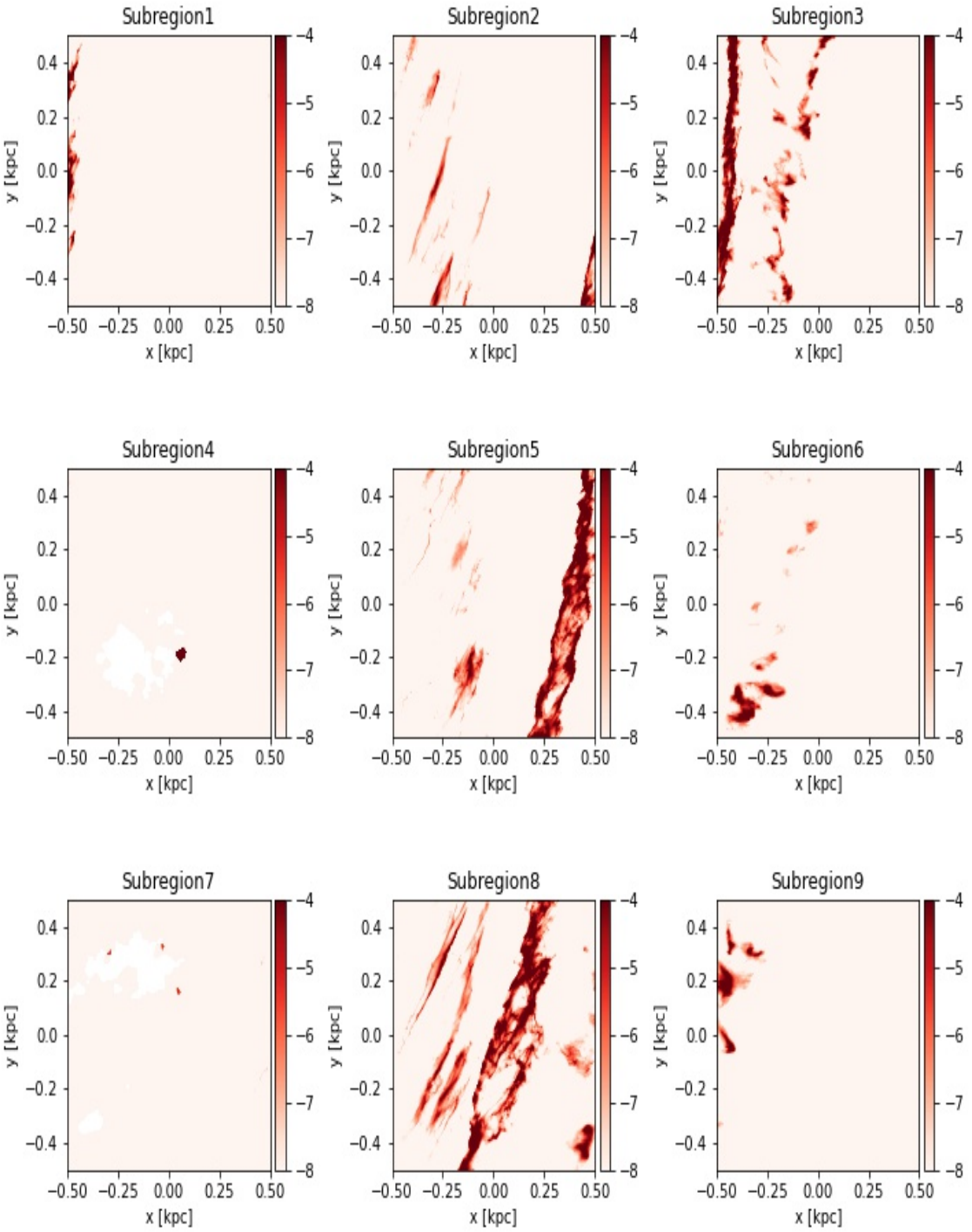

FIGURE 4.10: AREPO images showing the color scale of $\log_{10}(Z_{CO})$ for all 9 regions.

part, which results in the subregion of 500pc spatial resolution. Similarly, the 1kpc subregion is divided into 16, 100, and 200 parts consisting an equal number of AREPO cells in each to achieve 250pc, 100pc, and 50pc spatial resolutions of the subregions. The spatial resolutions for all the subregions are achieved in the same fashion. The column densities of CO, H_2, HI, and total column density are determined for the subregions at respective spatial resolutions by averaging over the AREPO cells pixel area, and the CO-dark gas fraction is estimated. The CO-dark gas fraction's behavior relative to the determined column densities is studied, and the sensitivity of the CO-dark gas fraction with the spatial resolutions of the AREPO image is investigated.

The mean of CO-dark gas fraction for different spatial resolutions relative to different column densities is presented using box plots (as the data set of the CO-dark gas fraction is randomly scattered), with $10^{0.5}$ cm^{-2} intervals by considering f_{dg} maximum of 0.98 (i.e., f_{dg} = 1, indicates that the complete H_2 is CO-dark). Then using equation 2.1, the CO to H_2 conversion factor is estimated for all the subregions at different resolutions. From Smith et al. (2020), Subregions 1, 4, and 7 represent the inter-arm, and Subregions 3, 6, and 9 represent the spiral arm of the simulation. Subregions 2, 5, and 8 represent the arm between the spiral arm and inter-arm; hence, it is called mid-arm regions in this thesis. The analysis and the outcomes of these methods are discussed in Section 5

Chapter 5

Results and discussion

5.1 CO observations

The velocity-integrated intensity is required to investigate the amount of H_2 gas that is not traced by CO(1-0). Using equation 4.3 the integrated intensity (W_{CO}) is determined. Figure 5.1 shows the plot of W_{CO}, where the color-scale represents the $\log_{10} W_{CO}$ K kms^{-1}. The region where W_{CO} is less than 0.1 K kms^{-1} indicates the CO-dark gas. From Figure 4.4 and Figure 5.1, it can be seen that the CO-dark gas surrounds the CO-bright gas in envelopes, especially in the mid-arm subregions. In inter-arm subregions, CO-dark gas is found in filamentary form, and in spiral-arm CO-dark gas is found in extended filamentary form and does not surround the CO-bright gas regions. With the help of Figure 4.10, which shows the distribution of column-averaged CO abundance for all the sub-regions, it can be seen that the region with $Z_{CO} \approx 10^{-4}$ we observe more CO emission from those regions (Figure 5.1). However, for subregion 3, Z_{CO} is seen to be high at the edges of the arm, for which we observe less CO-emission. There is some inconsistency for subregion 3, for which the origin is unknown.

The relation of velocity integrated CO(1-0) intensity (W_{CO}) relative to N_{H_2} is shown in Figure 5.2, where it is observed that for all the subregions for $N_{H_2} \geq 10^{19}$ cm^{-2} there is a strong increase in W_{CO} and for $N_{H_2} \geq 10^{21}$ cm^{-2} W_{CO} reaches the maximum CO intensity for all spatial resolutions. This is good agreement with the observations of Federman et al. (1980), Liszt & Lucas (1998) and Sheffer et al. (2008)). In general, it is observed that as the spatial resolution is increased, more CO is observed (CO-bright gas) in the subregions. From Figure 4.10 Subregion 4 and Subregion 7 has a very little Z_{CO} for which in Figure 5.2 it is observed that W_{CO} is around 10 Kkms^{-1} for Subregion 4 at low N_{H_2} ($\approx 10^{19}$ cm^{-2}) and for Subregion 7 W_{CO} is much less than 0.001 K kms^{-1}.

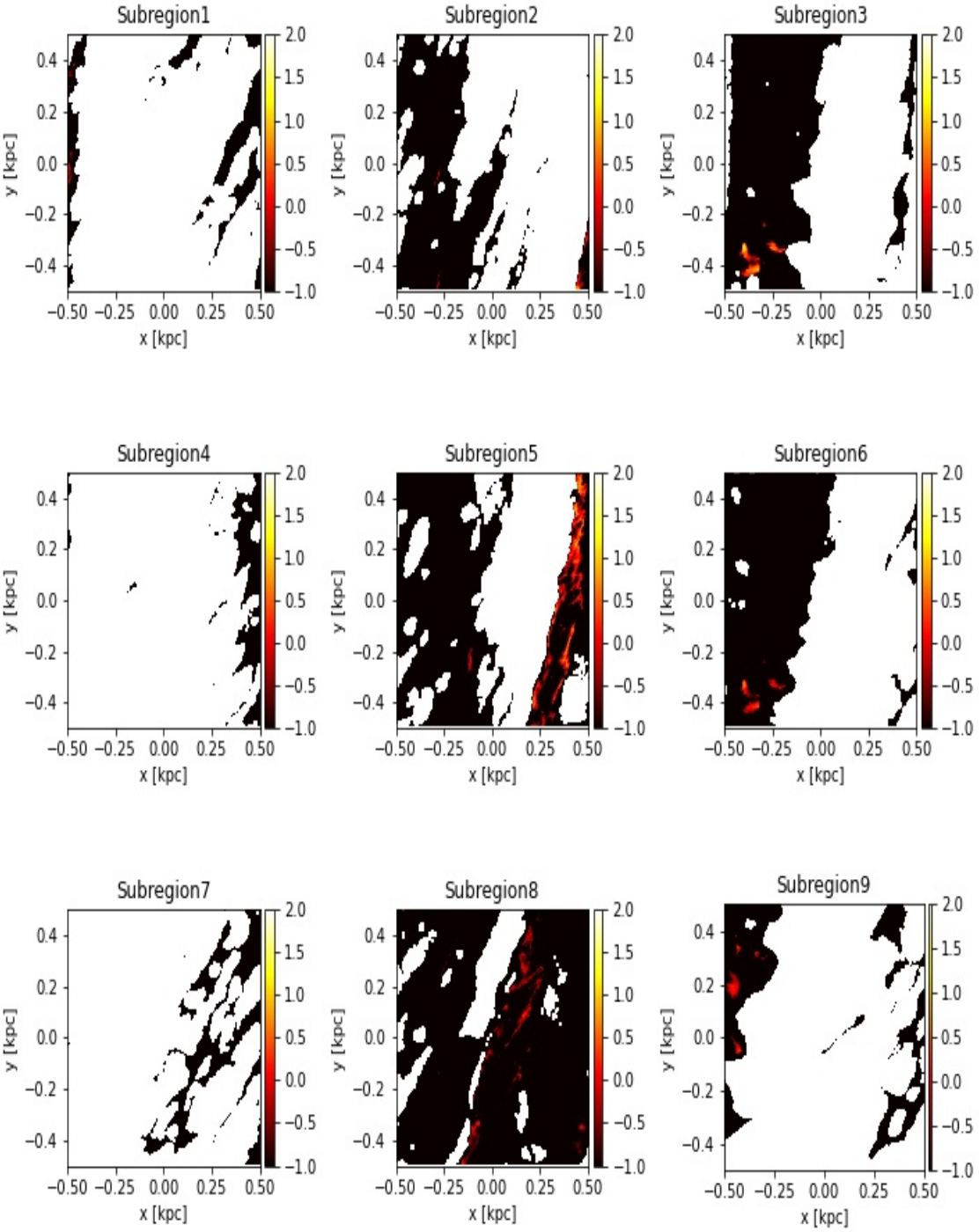

FIGURE 5.1: Log_{10} W_{CO} K kms^{-1} from each subregions which 1kpc across. $W_{CO} >$ 10 K kms^{-1} is CO-bright gas and $W_{CO} <$ 10 K kms^{-1} is CO-dark gas. The image resolution of each subregion is 1kpc. CO-dark gas surrounds the CO-bright gas regions in the mid-arm subregions especially. In the inter-arm subregions, CO dark regions are in filamentary form. In sprial-arm subregions, CO-dark gas does not entirely surround the CO-bright gas in the form of an envelope.

5.1.1 CO-dark gas fraction

H_2 molecular gas fraction, which is not traced by CO (CO-dark gas fraction), is calculated using the equation 4.6. The velocity-integrated CO(1-0) intensity visibility limit is discussed in the previous section (4.2). Figure 5.3 shows the CO-dark gas fraction as a function of W_{CO} for all spatial resolutions for the overall $10M_{\odot}$. It is observed that the qualitative shape of the curve remains the same only for 500pc and 1kpc resolutions and not for 250pc, 100pc, and 50pc spatial resolutions, where the curve starts increasing before reaching $W_{CO,th} < 10$ K kms^{-1}. The total molecular gas mass between the $W_{CO} > 0.1$ K kms^{-1} and $W_{CO,th} < 10$ K kms^{-1} is around 75%, 65% and 55% for 50pc, 100pc and 250pc spatial resolutions. Thus, assumption of $W_{CO,th} < 10$ K kms^{-1} depends on the spatial resolution. If the new threshold value is considered as $W_{CO,newth} < 1$ K kms^{-1}, it is found that between the sensitivity limit ($W_{CO,th} < 0.1$ K kms^{-1}) and $W_{CO,newth}$ is around 3%, 5% and 4% of the total molecular mass is present. Assuming the new integrated intensity threshold as $W_{CO,newth} < 1$ K kms^{-1} (shown in grey line in Figure 5.3) the CO-dark gas fraction are 0.01 - 0.34, 0.15 - 0.32, 0.1 - 0.24, 0.22 and 0.36 for 50pc, 100pc, 250pc, 500pc, and 1kpc spatial resolutions respectively for the overall $10M_{\odot}$ resolution region. The choice of the threshold influences the CO-dark gas fraction.

Figure 5.4 shows the variation of H_2 mass below the W_{CO} for the subregions, by adopting $W_{CO,newth}$ (shown in grey line in the Figure). From Figure 5.2, it is clear that more CO is detected in subregions for high spatial resolutions. Table 5.1 shows that as the spatial resolution increases, the range of CO-dark gas fraction varies in huge amounts. It is seen that the lower limit of the CO-dark gas fraction range increases as the spatial resolution is decreased for all the spatial resolutions.

TABLE 5.1: H_2 mass below $W_{CO,newth} < 1$ K kms^{-1} for all spatial resolutions. Subregion 7 shows 100 % CO-dark gas mass as there is much less CO emission observed in this subregion.

Region	50pc	100pc	250pc	500pc	1kpc
Subregion 1	8%	14%	25 %	32%	39%
Subregion 2	6% -20%	10 %-20%	21%	35%	97%
Subregion 3	15% -30%	51% -60%	90%	98%	99%
Subregion 4	64% -90%	69% -90%	86%	91%	94%
Subregion 5	0.1%	5% -10%	5%	19%	25%-62%
Subregion 6	6%-30%	25%	42%	66%	66%
Subregion 7	100%	100%	100%	100%	100%
Subregion 8	2.1%	10%	22%	57%	46%
Subregion 9	15%-22%	31% -40%	41%	59%	56%

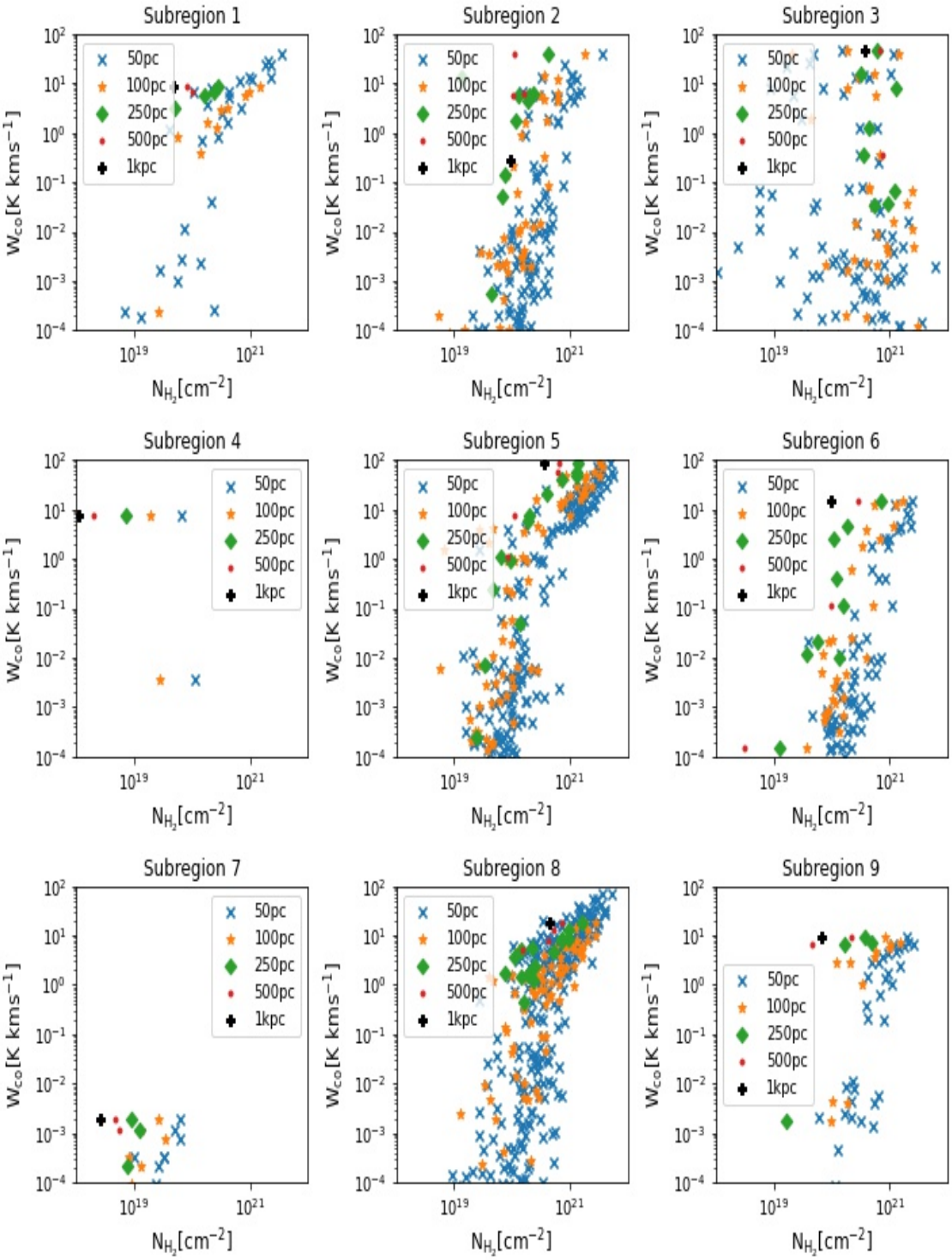

FIGURE 5.2: W_{CO} Kkms^{-1} as a function of N_{H_2} cm^{-2}. W_{CO} is less than 1 Kkms^{-1} for $N_{H_2} < 10^{21}$ cm^{-2} i.e, where the CO-dark gas is found generally. This holds true for all the spatial resolutions where 50pc and 100pc spatial resolutions saturates at higher N_{H_2} cm^{-2}. Subregion 7 as CO-dark gas at much low N_{H_2} ($< 10^{20}$) cm^{-2}.

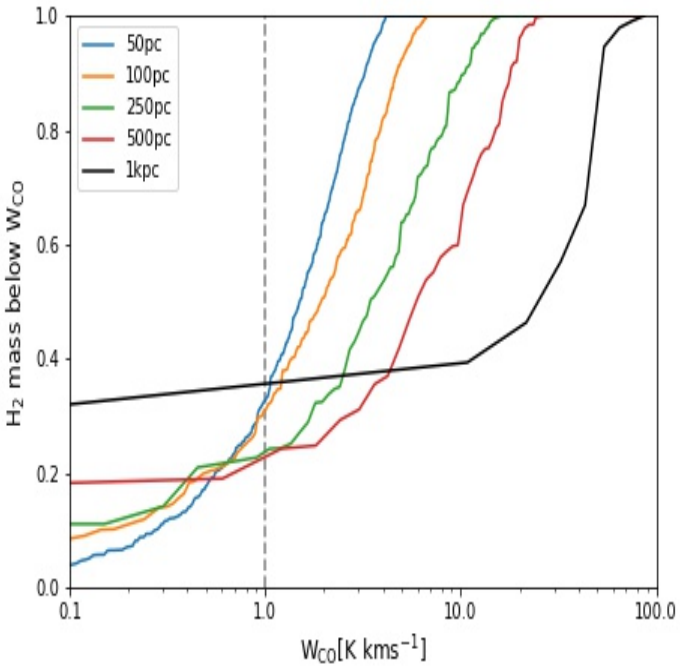

FIGURE 5.3: H_2 mass below W_{CO} for $10M_{\odot}$ region for different spatial resolutions. For 1kpc and 500pc spatial resolution, CO dark gas mass remains almost the same upto $W_{CO,th}$. $W_{CO,newth}$ is indicated by grey line.

5.2 CO-dark gas fraction's relation with column densities

CO-dark gas fraction's behavior, along with the column densities, is investigated by plotting f_{dg} against the column densities. Figures 5.5, 5.6, 5.7 and 5.8 show the relation of CO-dark gas fraction with CO column density (N_{CO}), H_2 column density (N_{H_2}), HI column density (N_{HI}) and total column density (N_{SD}) for 50pc (top left),100pc (top right), 250pc (middle left), 500pc (middle right) and 1kpc (bottom) spatial resolutions for the respected figures.

From Figure 5.5 it is observed that between the CO column densities of 10^{15}-10^{17} cm^{-2} there is a variation of CO-dark gas fraction that is being observed. This is in good agreement with the findings of Smith et al. (2014) that there is no significant CO emission for CO column densities less than 10^{16} cm^{-2}. This is the column density range in which we can expect the CO-dark gas fraction to be found. Figure 5.6 it can be seen that for N_{H_2} values in the range from $10^{18} - 10^{22}$ cm^{-2} for all the resolutions. This is in good agreement with the values of Planck Collaboration et al. (2011a). They have found that the CO-dark gas fraction is found at 10^{20} cm^{-2} $<N_{H_2}<10^{21}$ cm^{-2}. It is observed that from Figure 5.7 that

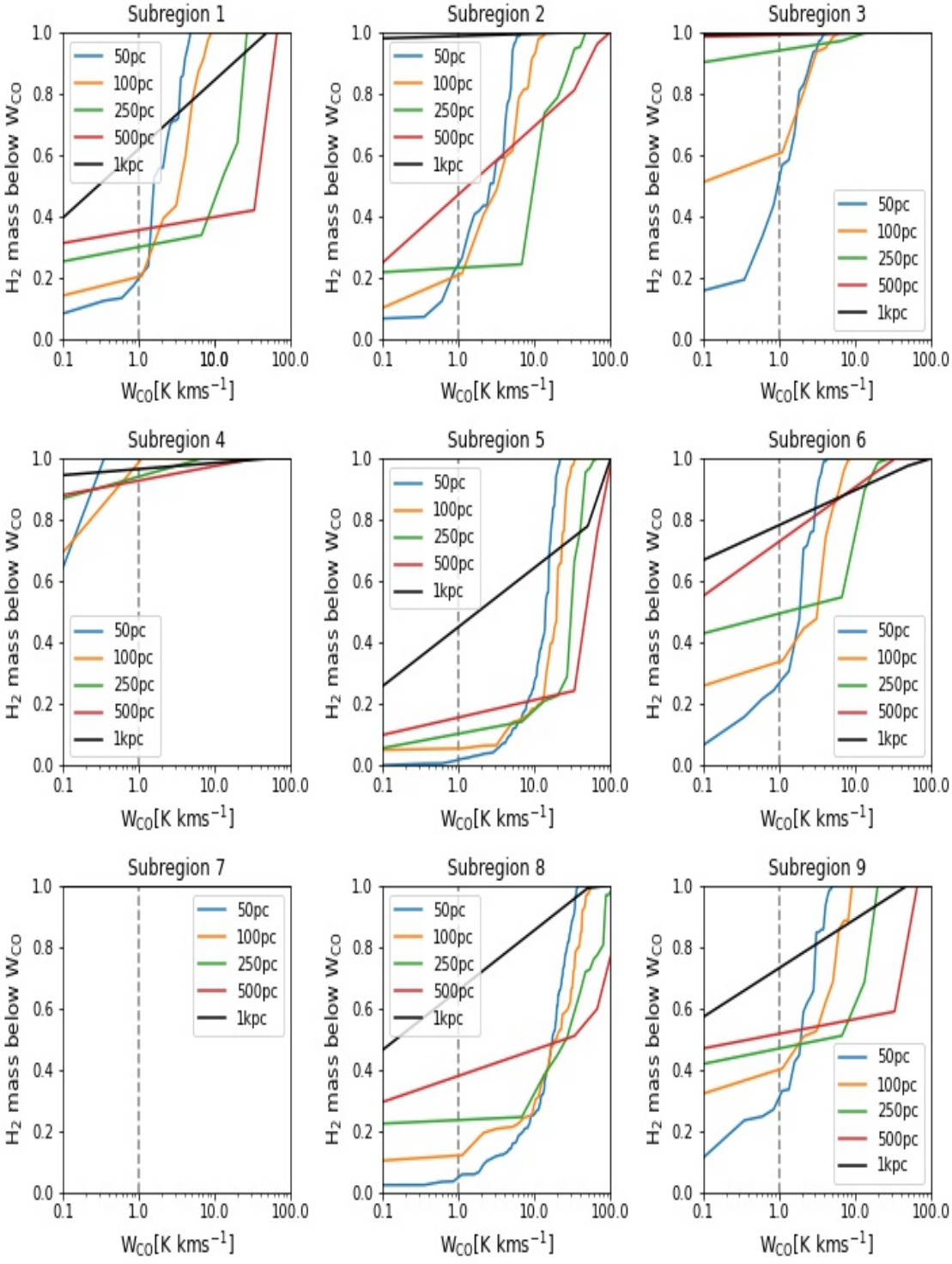

FIGURE 5.4: CO-dark gas fraction (with $W_{CO,newth}$ as the threshold value, represented in grey line) as a function of W_{CO} K kms^{-1} for all the Subregions at different spatial resolutions. CO-dark gas fraction is sensitive to the spatial resolution at which the AREPO image is studied. For Subregion 7 H_2 mas is found at W_{CO} is much less than 0.1 K kms^{-1}

the scatter in CO-dark gas fraction is huge for N_{HI} in the range 10^{20} cm^{-2} - 10^{22} cm^{-2}. From Figure 5.8, CO-dark gas fraction is found to be high at the lower surface density of the interstellar gas and scattered for N_{sd} in the range 10^{20} cm^{-2} - 10^{22} cm^{-2}. This is because the shielding of the molecular gas reduces along with the surface density, which results in CO photodissociation. All these plots show that as the spatial resolution of the AREPO image is decreased, the CO-dark gas fraction is not observed completely.

5.2.1 Box plots of N_{H_2}, N_{HI} and N_{SD}

CO-dark gas fraction scattered along with column densities (Figures 5.5 - 5.8) where it is not possible to arrive at the general relation between the column densities and CO-dark gas fraction. Thus, to understand the behavior of CO-dark gas fraction, the column densities values are binned in $10^{0.5}$ cm^{-2} intervals, and the box plots for these intervals are plotted, 1kpc spatial resolution sub-regions have one data-value per subregion (by the definition of increasing the spatial resolution), and hence, this method is implied for 1kpc spatial resolution. Figures 5.9, 5.10 and 5.11 represents the boxplots of f_{dg} relative to N_{H_2}, N_{HI} and N_{sd} respectively for 50pc, 100pc, 250pc and 500pc resolution.

The width of each box indicates the interval's size, and the box plots' length shows the variation of f_{dg} in the intervals. If the box is absent, then it means that there is no variation in f_{dg} value (i.e., there is only one f_{dg} value in that interval). The green triangle and the green line in the box plot are the mean and median of f_{dg} in the respective intervals. The small circles in the plots are the outliers which show that there might be some f_{dg} present at that value. The red color square box indicates the +1σ, and the blue color square box represents the -1σ value meaning that the 66% of the f_{dg} present considering mean of the data set as the center value. If the median is present above the mean, it is known as left skewed; if the mean is above the median, it is known as right skewed. The data set is not symmetrical if the data is either right-skewed or left-skewed.

From Figure 5.9, it is seen that there is a huge variation in the f_{dg} in each interval. For 50pc spatial resolution, the f_{dg} is left skewed up to $N_{H_2} = 10^{20.5}$ cm^{-2} meaning that the f_{dg} values are closer above the median whereas it is spread at below the median. For $N_{H_2} = 10^{21}$ cm^{-2} and $10^{21.5}cm^{-2}$ f_{dg} is equally distributed above and below the median. For 100pc spatial resolution, the data is left skewed lower column densities. For 250pc the data is right skewed and at $N_{H_2} = 10^{18.5}$ cm^{-2} and 10^{19} cm^{-2} there is no variation in f_{dg}. For 500pc, The data is almost symmetrical. It can be seen that as the spatial resolution of the subregions is

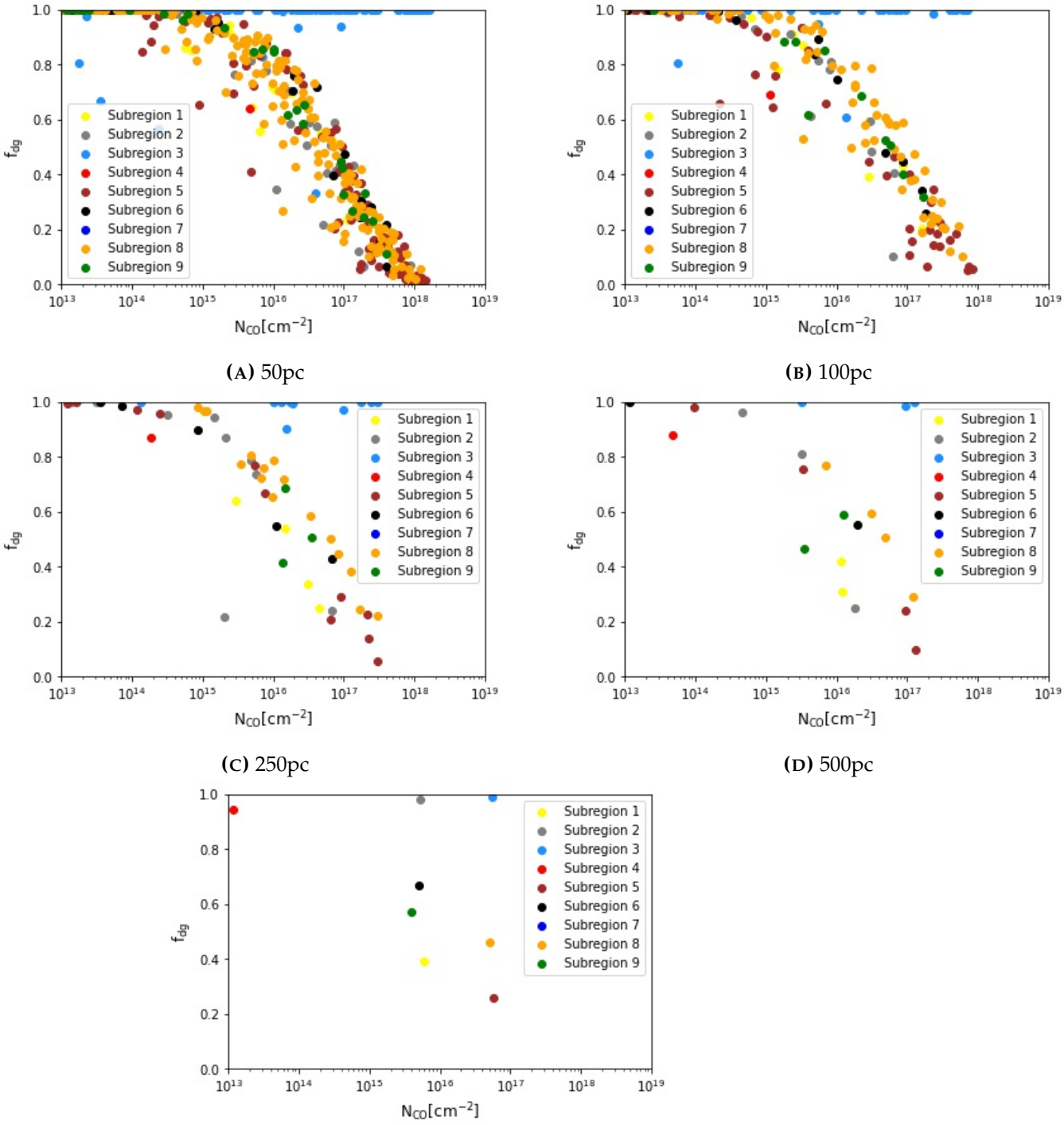

(A) 50pc

(B) 100pc

(C) 250pc

(D) 500pc

(E) 1kpc

FIGURE 5.5: CO-dark gas fraction against $N_{CO}[cm^{-2}]$ for all 9 subregions at different spatial resolutions.

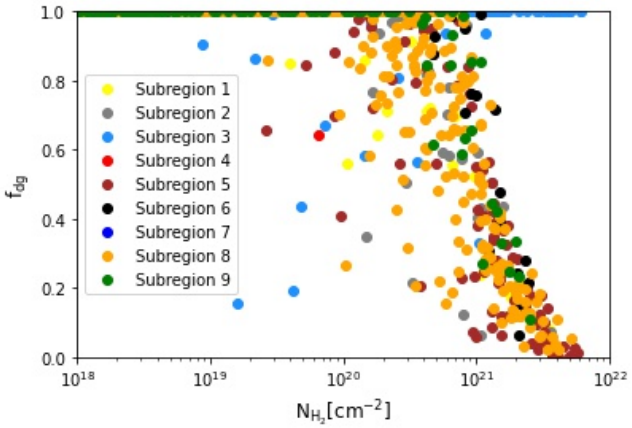

(A) 50pc

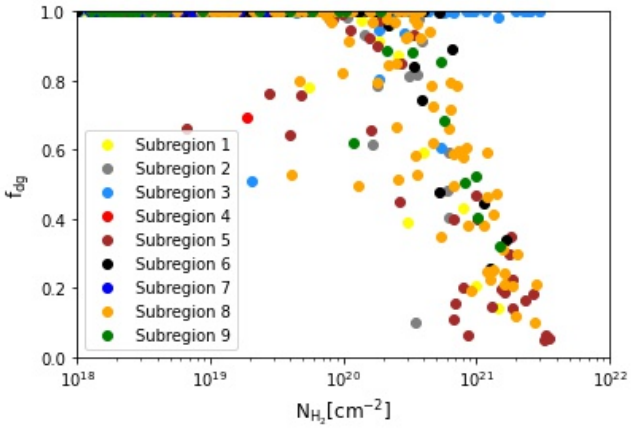

(B) 100pc

new

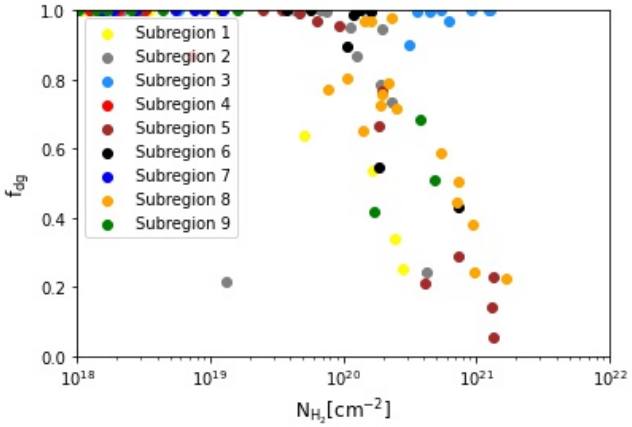

(C) 250pc

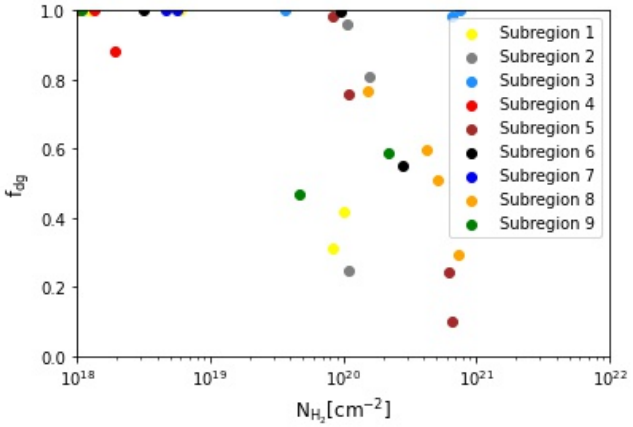

(D) 500pc

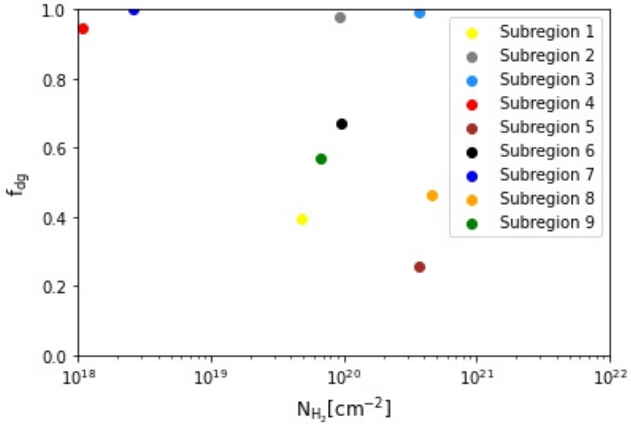

(E) 1kpc

FIGURE 5.6: CO-dark gas fraction against $N_{H_2}[cm^{-2}]$ for all 9 subregions at different spatial resolutions.

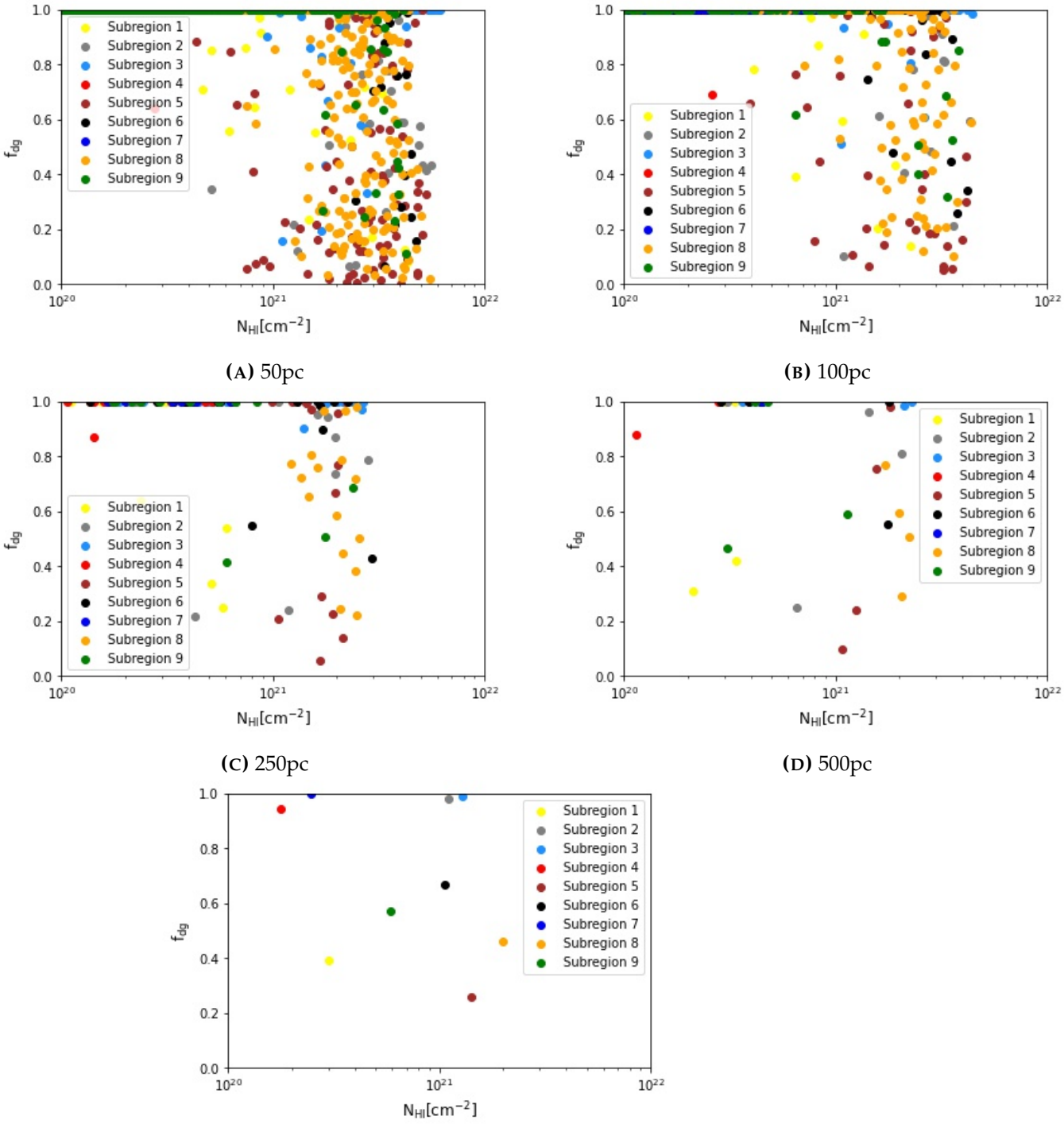

(A) 50pc

(B) 100pc

(C) 250pc

(D) 500pc

(E) 1kpc

FIGURE 5.7: CO-dark gas fraction against $N_{HI}[cm^{-2}]$ for all 9 subregions at different spatial resolutions.

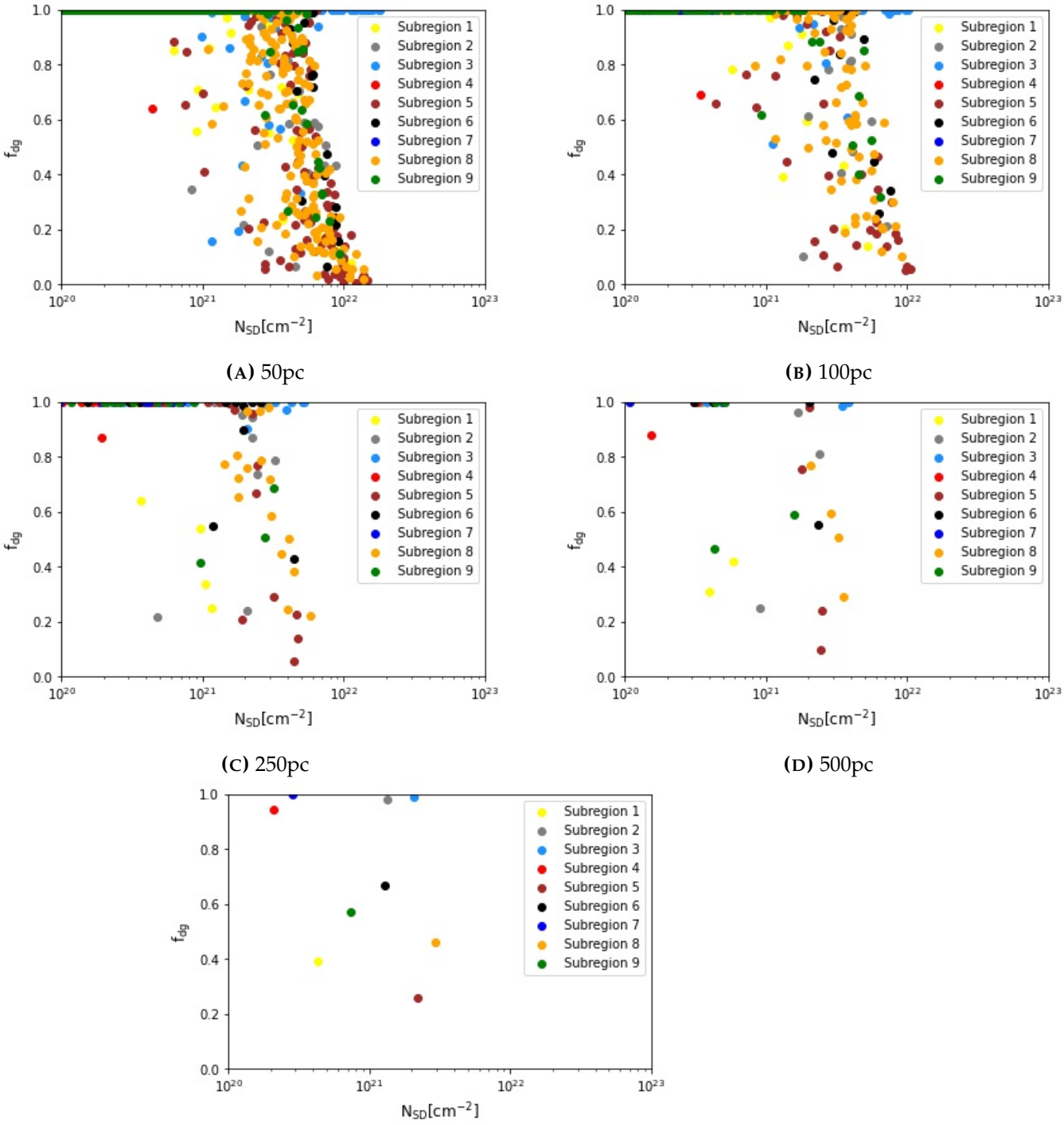

(A) 50pc

(B) 100pc

(C) 250pc

(D) 500pc

(E) 1kpc

FIGURE 5.8: CO-dark gas fraction against $N_{SD}[cm^{-2}]$ for all 9 subregions at different spatial resolutions.

increased, the f_{dg} is spread over a wide range of N_{H_2}. However, as the spatial resolution is decreased, the variation of f_{dg} is observed at 10^{20} cm^{-2} $\leq N_{H_2} \leq$ 10^{21} cm^{-2}. The data at high column densities of each interval the data is symmetrical. At a given N_{H_2}, it is observed that CO-dark gas fraction varies without any general trend. Hence, by these plots, it can be said that there is no general behavior of f_{dg} with N_{H_2} between these spatial resolutions or in other words f_{dg} is dependent on the spatial resolution of the AREPO image with no general trend between the spatial resolutions.

Figure 5.10 represents the box plots for f_{dg} relative to N_{HI}. For 50pc spatial resolution, the mean values are almost consistent, and the f_{dg} is both right and left-skewed. For 100pc spatial resolution, the mean values decrease as the column density increases. For 250pc and 500pc spatial resolutions f_{dg} are left skewed for N_{HI} = 10^{21} cm^{-2} and symmetrical for N_{HI} = 10^{20} cm^{-2}. The mean values of CO-dark gas fraction remain close to each other for 50pc and 100pc spatial resolution, whereas for 250pc and 500pc spatial resolution, the mean CO-dark gas fraction shows a similar trend. From Figures, 4.4 and 4.5, the regions with high H_2 column densities consist of high HI column densities as well. As the spatial resolution increases, we observe more gas consisting of HI and CO. However, for a given N_{HI}, the mean CO-dark gas fraction varies depending on the spatial resolution.

Figure 5.11 represents the box plots for f_{dg} relative to N_{sd} intervals. For 50pc spatial resolution, all the data sets are right skewed, and for 100pc spatial resolution, the data is both right and left skewed. For 250pc and 500pc spatial resolutions $f_{dg}$is left skewed for $N_{sd} \leq 10^{21}$ cm^{-2} whereas for N_{sd} = 10^{21} cm^{-2} the data are symmetrical. From Figure 4.7, it is noticed that at the spatial resolution is increased, the fraction abundance of H_2 reduces to less than 0.5. We know that at high spatial resolutions, we detect more CO. This leads to the variation of CO-dark gas fraction along N_{sd} such that at a given N_{sd} CO bright gas is observed more and H_2 fractional abundance is less at high spatial resolutions.

Overall for all these box plots, it can be understood that f_{dg} is dependent on the spatial resolutions of the AREPO images, and there is no general trend between different resolutions. At higher N_{H_2}, N_{HI} and N_{sd} f_{dg} is symmetrical or close to symmetry.

5.3 CO to H_2 conversion factor (X_{CO})

The observed velocity integrated CO emission is used to determine X_{CO} using the equation 2.1. X_{CO} is calculated here by considering W_{CO} greater than 0.1 K

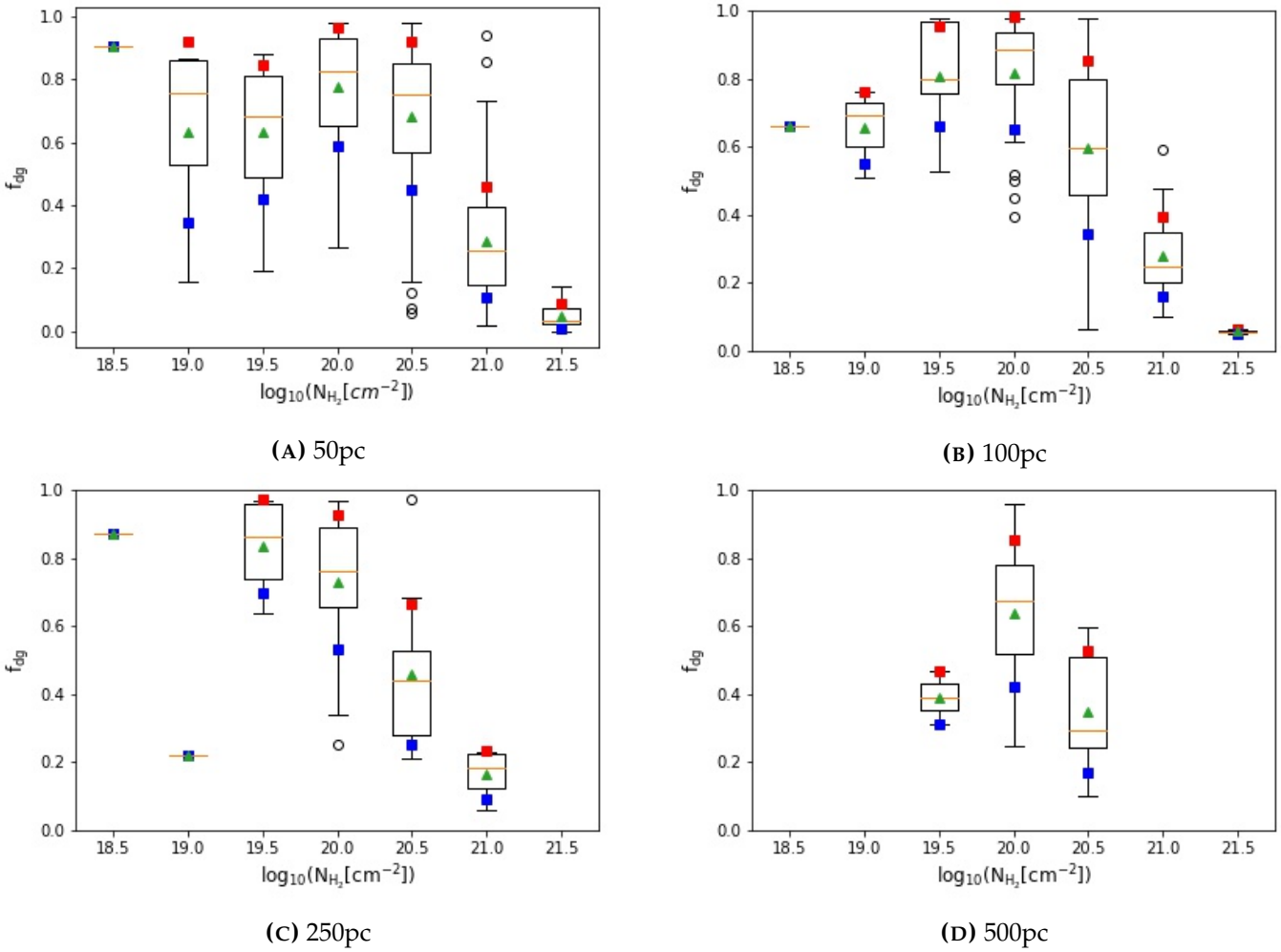

(A) 50pc

(B) 100pc

(C) 250pc

(D) 500pc

FIGURE 5.9: Box plot of CO-dark gas fraction against $\log_{10}(N_{H_2}\ [cm^{-2}])$ intervals for 50pc, 100pc, 250pc and 500pc spatial resolution of the subregions showing $\pm$ 1 σ values of f_{dg} in the interval. The green triangle and the green line inside the boxplot indicate the mean and median of the distribution of the respective interval, respectively. The red square box shows the +1σ value, whereas the blue box shows the -1σ value.

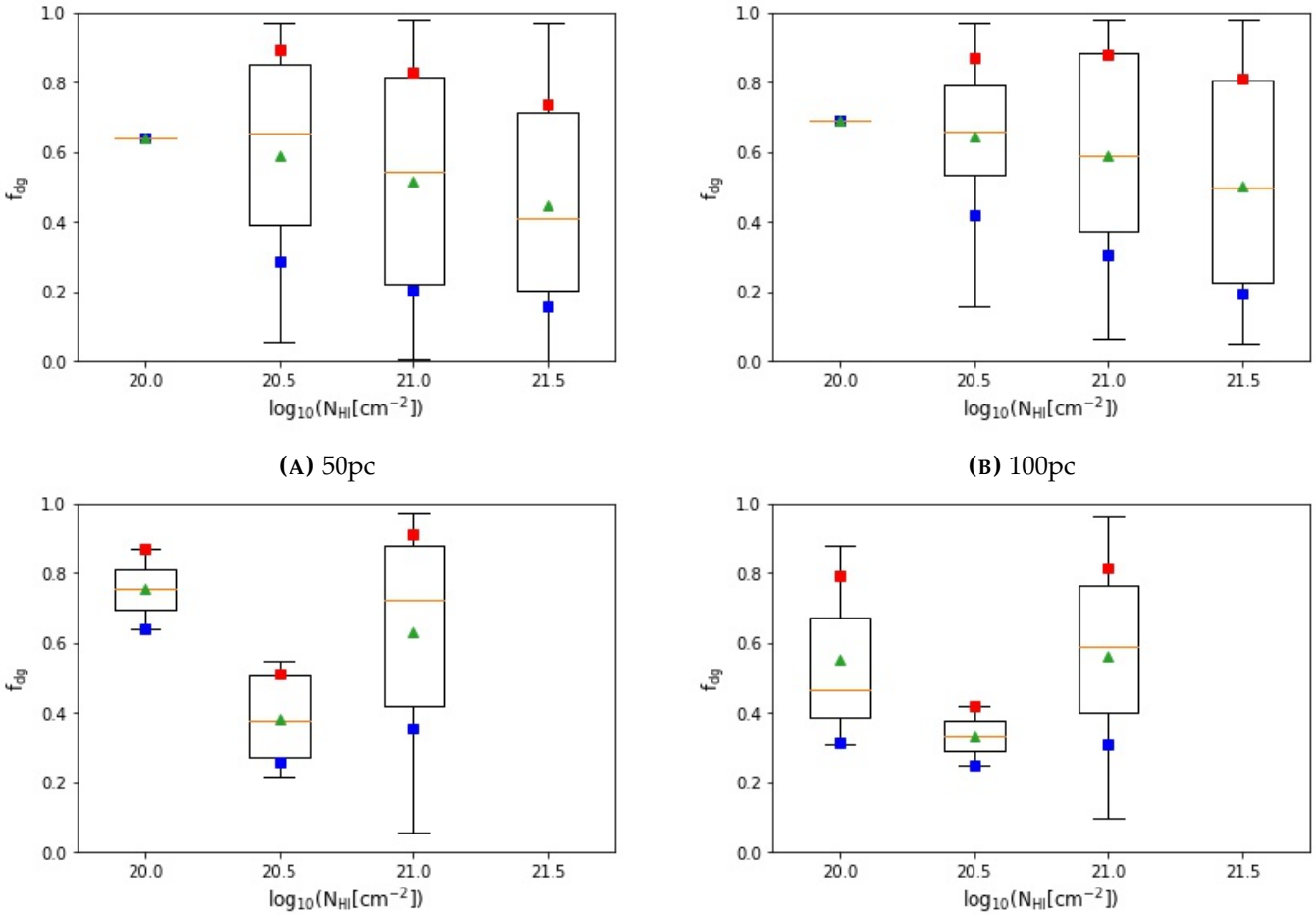

(A) 50pc

(B) 100pc

(C) 250pc

(D) 500pc

FIGURE 5.10: Box plot of CO-dark gas fraction against $\log_{10}(N_{HI}\ [cm^{-2}])$ intervals for 50pc, 100pc, 250pc and 500pc spatial resolution of the subregions showing $\pm$ 1 σ values of f_{dg} in the interval. The green triangle and the green line inside the boxplot indicate the mean and median of the distribution of the respective interval, respectively. The red square box shows the +1σ value, whereas the blue box shows the -1σ value.

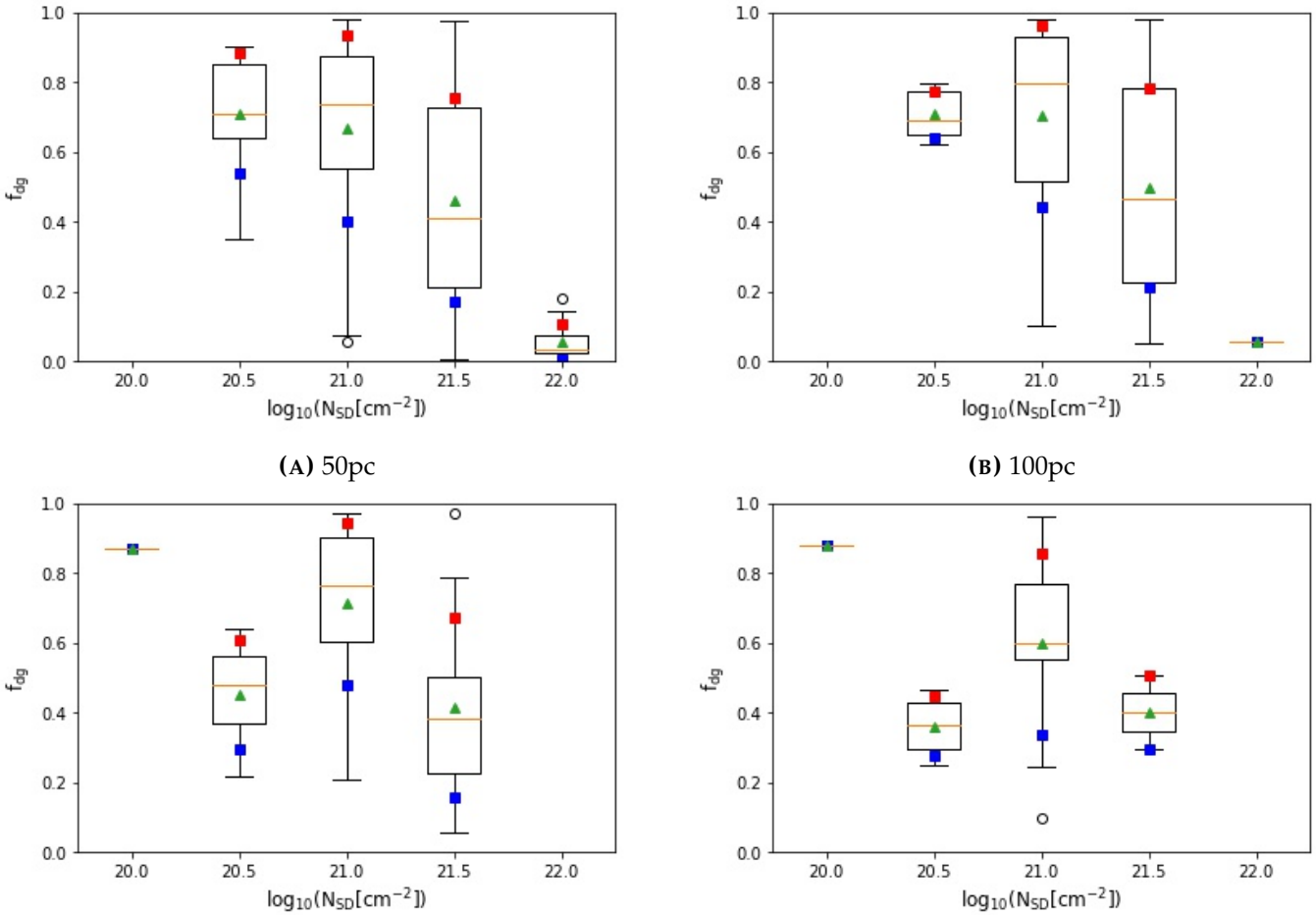

(A) 50pc

(B) 100pc

(C) 250pc

(D) 500pc

FIGURE 5.11: Box plot of CO-dark gas fraction against $\log_{10}(N_{sd}\ [cm^{-2}])$ intervals for 50pc, 100pc, 250pc and 500pc spatial resolution of the subregions showing $\pm$ 1 σ values of f_{dg} in the interval. The green triangle and the green line inside the boxplot indicate the mean and median of the distribution of the respective interval, respectively. The red square box shows the +1σ value, whereas the blue box shows the -1σ value.

kms^{-1} (CO is visible). The standard X_{CO} for Milky Way is adopted as $X_{CO,gal}$ = 2×10^{20} $cm^{-2}K^{-1}km^{-1}s$ in each pixel (Bolatto et al. (2013)). However, on a pixel basis, it is seen that the distribution of integrated intensities differs from a simple estimate of X_{CO}. H_2 column density increases X_{CO} decreases, which means that at low H_2 column densities, less CO emission is observed as the effect of CO-photodissociation. Such variation of the distribution of integrated intensities have been identified by Shetty et al. (2011) and individual GMCs observations by Pineda et al. (2008), where it has been presented that X_{CO} is a meaningful quantity when the emission and the H_2 column density on scales comparable to or larger than the typical size scale of individual GMCs (see the discussion on this statement from Bolatto et al. (2013)). Accordingly, when the emission and H_2 column density is averaged for over all 10 $M_\odot$ resolution region the X_{CO} values that are obtained are 3.4×10^{20} $cm^{-2}K^{-1}km^{-1}s$ for 50pc spatial resolution, 2.5×10^{20} $cm^{-2}K^{-1}km^{-1}s$ for 100pc resolution, 1.4×10^{21} $cm^{-2}K^{-1}km^{-1}s$ for 250pc resolution, 1.7×10^{20} $cm^{-2}K^{-1}km^{-1}s$ for 500pc resolution and 1.9×10^{20} $cm^{-2}K^{-1}km^{-1}s$ for 1kpc resolution.

Figure 5.12 shows the variation of X_{CO} $cm^{-2}K^{-1}km^{-1}s$ along with N_{H_2} cm^{-2}. In section 5.1, it was observed that at the spatial resolution, there is high CO emission observed (Figure 5.2) which affects the CO-H_2 conversion factor. From Figure 5.12 it is seen that X_{CO} varies along the spatial resolution for a given H_2 column density. Table 5.2 consists of the globally averaged X_{CO} values for each subregion at different resolutions. X_{CO} values increase as the spatial resolution is decreased. For 50pc and 100pc resolutions, X_{CO} are closer to the canonical Galactic value for the Milky Way, X_{CO} = 2.2 $\times 10^{20}$ $cm^{-2}K^{-1}km^{-1}s$, whereas for other spatial resolutions X_{CO} values are approximately higher by a factor of 1-3. This variation of X_{CO} is in good agreement with the observational results of galactic and extragalactic MCs (Blitz & Shu (1980), Leroy et al. (2007), Scoville et al. (1987), Strong & Mattox (1996), Lombardi et al. (2006), Nieten et al. (2006)). For subregion 4 the derived globally averaged X_{CO} is one order magnitude lower than the $X_{CO,gal}$ at all resolution because it is observed that CO is detected at low N_{H_2}. and for 1kpc spatial resolution of all the subregions, the derived globally averaged X_{CO} is found to be 1-3 orders of magnitude lower than $X_{CO,gal}$, this is due to the obscuration of N_{H_2} (5.6) at this resolution and CO (5.2). It is observed that for all the subregions, the X_{CO} values depend on the spatial resolution observed for a given H_2 column density.

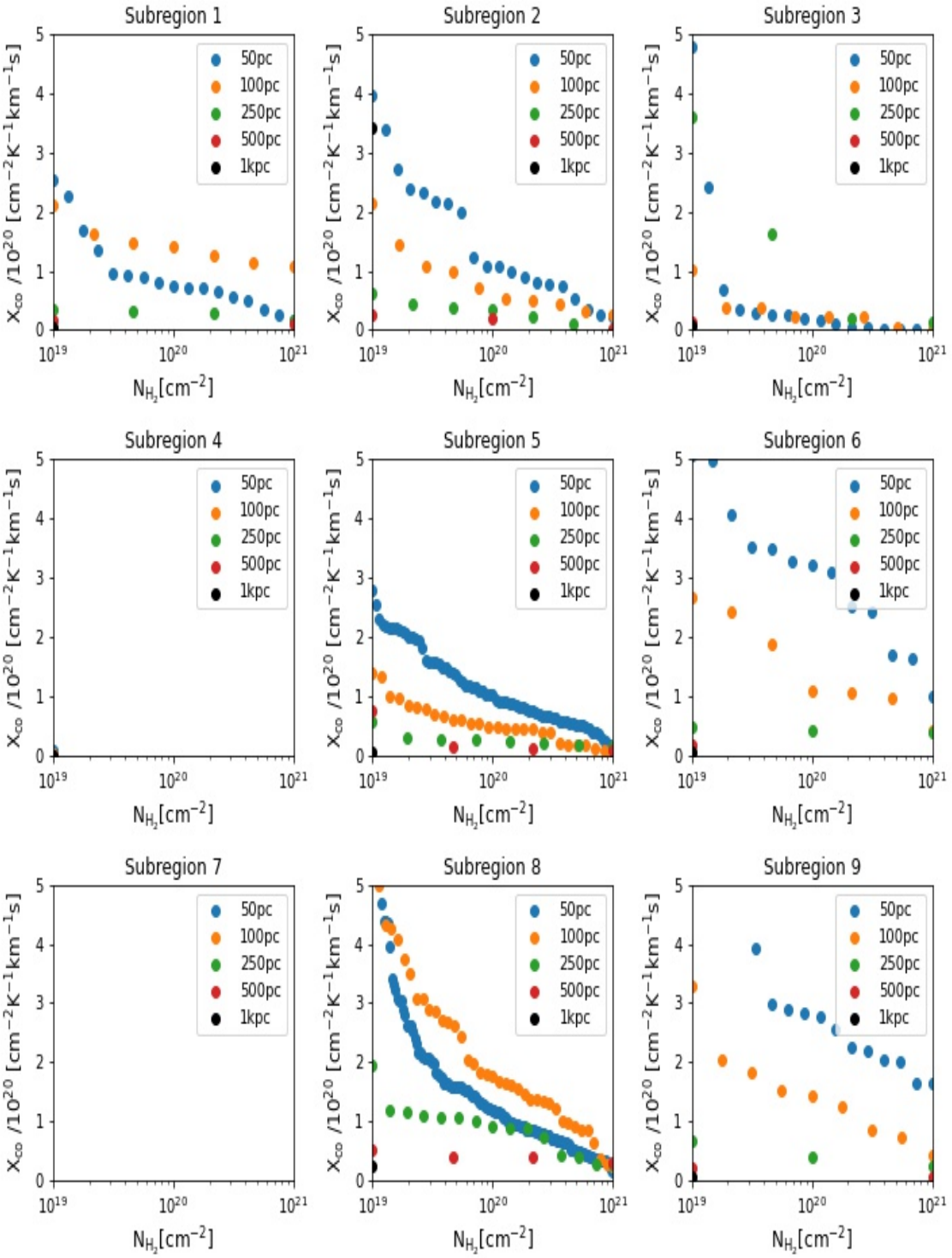

FIGURE 5.12: Globally averaged X_{CO} as a function of N_{H_2} for all subregions at different spatial resolutions. For subregion 4 and subregion 7 W_{CO} is much less tha 0.1 K kms^{-1}. Therefore, the X_{CO} is not seen.

TABLE 5.2: X_{CO} values for all the subregions for different spatial resolutions by considering only the integrated intensities $W_{CO} > 0.1$ K kms^{-1} where CO is visible. For subregion 7 there is no X_{CO} determined as this subregion shows no CO emission > 0.1 K kms^{-1} (see Figure 5.2)

Region	50pc	100pc	250pc	500pc	1kpc
Subregion 1	2.3×10^{20}	2.6×10^{20}	3.17×10^{20}	5×10^{20}	5.3×10^{18}
Subregion 2	2.3×10^{20}	2.4×10^{20}	2.6×10^{20}	3.7×10^{20}	3×10^{20}
Subregion 3	2.3×10^{20}	2.5×10^{20}	3.1×10^{20}	1×10^{19}	7×10^{18}
Subregion 4	1×10^{19}	1×10^{19}	1×10^{19}	1×10^{19}	1.4×10^{17}
Subregion 5	2.1×10^{20}	2.2×10^{20}	2.5×10^{20}	3.1×10^{20}	2.5×10^{19}
Subregion 6	2.3×10^{20}	2.6×10^{20}	3.7×10^{20}	1×10^{19}	6.3×10^{18}
Subregion 7	-	-	-	-	-
Subregion 8	2.1×10^{20}	2.2×10^{20}	2.3×10^{20}	3.1×10^{20}	2.5×10^{19}
Subregion 9	2.3×10^{20}	2.5×10^{20}	3.7×10^{20}	5×10^{20}	6.9×10^{18}

5.4 Sources of uncertainties

The potential uncertainties in the simulation of the model are as follows: The assumption of uniform interstellar radiation field (ISRF) is false for the regions closer to massive star formation on small scales; however, it is a reasonable assumption on large scales as it is being taken in a region within a few kpc of the Solar Galactocentric radius Wolfire et al. (2010). Another assumption of constant shielding length of 30pc between the gas and the radiation source for the overall simulation. If the star formation is clustered, the cluster mass increases with star formation, for which a constant shielding length is a reasonable approximation. However, if the star formation density is constant, this shielding length will be smaller for higher field strengths and converse. For Milky Way, there are some questions regarding the assumption that this shielding length might be shorter for spiral arms. To perform a full parameter study, the simulation is too expensive computationally; however, a first estimate of the local shielding length may be represented by the shielding length assumed for this simulation. A constant metallicity and dust-to-gas ratio are assumed for the simulation, but the Milky Way galaxy has a slight gradient in the metallicity with a Galactocentric radius. The model on which this thesis is performed uses an external potential to produce tightly wound spiral arms and does not include the effects of self-gravity or stellar feedback, which is an idealized treatment of the galaxy. The plausible explanation for why the Galaxy's star formation efficiency is so low is due to maintaining the molecular clouds in a gravitationally unbound state by the energy input from stellar feedback Dobbs et al. (2008a).

Additional uncertainty might be produced because of the treatment of CO

chemistry, which is approximate and tends to underpredict the actual CO abundance along the very low column density sight lines, which leads to the approximate method for determining W_{CO}. However, neither of these uncertainties do strongly affect the results that are derived for CO-dark gas fraction. This is because there is a substantial increase in the CO emission from CO-bright compared to CO-dark gas, which is far beyond the uncertainties.

5.5 Caveats

Magnetism is an essential physical process that is not included in the simulation of the model. It is known that molecular clouds (Crutcher (2012)) and galaxies (Beck et al. (2013) have of magnetic fields which affect the cloud formation and fragmentation within them. Therefore, not including the magnetic fields is an important caveat. Another caveat is that only supernova feedback is only used. At the same time, it is known that stellar winds, photoionization, and radiation pressure also play essential roles in shaping the cold interstellar medium. Simulations produced by Hopkins et al. (2012) where these processes are included do not follow the cold molecular phase of the ISM in detail at the resolution in which the simulations are carried out to produce the model that is used in this thesis. Therefore, for simplicity and computational efficiency, these processes are neglected in the simulation model used in this thesis.

Chapter 6

Comparison with previous work

For individual clouds Wolfire et al. (2010) have used PDR models of the spherical clouds to estimate the amount of H_2 that is present in the CO-dark cloud envelope. Wolfire et al. (2010) have arrived at the value of f_{dg} as 0.3 with the exact definition of f_{dg} as in this thesis, which is slightly sensitive to mass or interstellar radiation field for the cloud which has mean extinctions characteristic of observed GMC's. The value of f_{dg} = 0.36 for 1kpc spatial resolution for overall $10M_{\odot}$ resolution region is in good agreement with this. Wolfire et al. (2010) also shown that f_{dg} is a function of visual extinction of the cloud, i.e., f_{dg} increases as the mean extinction decreases. In the Milky Way simulation, which produces the model used in this thesis, a significant amount of total H_2 gas is located in the long filamentary clouds, as the effect of their geometry it tends to have low visual extinction and hence high f_{dg} as the spatial resolution is increased. As the spatial resolution is decreased, these regions of clouds are also included, which provides a similar result with Wolfire et al. (2010)
One of the observational attempts to determine the f_{dg} is done by Grenier et al. (2005), where large-scale maps of HI and CO emission, dust emission, and extinction and γ-ray emission are used. They have estimated that a significant fraction of gas is traced by dust emission and absorption and also by γ- ray emission but was not traced by HI or CO emission. They derived that the total mass of f_{dg} to be 50% - 100% of the mass in CO-bright clouds. The definition for f_{dg} is as same as in this thesis. It corresponds to the f_{dg} values in the range 0.33-0.5. This is in good agreement for the f_{dg} arrived in this thesis for 1kpc resolution of overall $10M_{\odot}$ resolution region.

By constructing an all-sky map of dust temperature and optical depth and correlating this with HI and CO emission Planck Collaboration et al. (2011a) have investigated the CO-dark fraction (different definition for f_{dg} from the definition used in this thesis). The excess from the dust emission and comparing it with

the emission from the above tracers was estimated as the CO-dark gas. They have shown that this CO-dark gas was 118 % times that of the CO-bright gas (no clouds near the Galactic mid-plane is considered). This corresponds to the f_{dg} value of 0.54 when the definition for f_{dg} from this thesis is assumed. As the spatial resolution is increased we see the clouds more in-depth far away from the Galactic mid-plane which is probably a reasonable explanation for the variation of CO-dark gas fraction values as the spatial resolution is increased.
Furthermore, Paradis et al. (2012) have also performed a dust-based study using dust extinction maps rather than Plank far-infrared maps. They have estimated the CO-dark gas fraction of 0.62 (for high latitudes, $|b| > 10\,^{\circ}$). However, they have also shown that for inner galaxy f_{dg} is 0.71 and for outer galaxy f_{dg} is 0.43. My f_{dg} values for overall $10M_{\odot}$ with poor spatial resolutions are in good agreement.
Using [CII] emission as a tracer for CO-dark gas Pineda et al. (2013) have performed an observational study to look for the structures in the distribution of CO-dark gas fraction. They have used GOT C+ (Galactic Observations of Terahertz C^{+}) survey (Langer et al. (2010b) to study the distribution of [CII] emission in the Milky Way. With utilising the Heterodyne Instrument for the Far Infrared (de Graauw, Th. et al. (2010)) on board Herschelspace telescope (Pilbratt et al. (2010)), they have collected 500 evenly distributed lines of sight in the Galactic plane, which were observed at 158 μm and by correlating the detected [CII] emission with complementary maps of HI and CO emission they have recognized the regions with excess [CII] emission which was not explained from the atomic cloud or CO-bright molecular clouds. This excess [CII] emission is interpreted as emission from CO-dark clouds. By averaging their complete survey, they estimated f_{dg} as 0.3 and also determined that it varies substantially with Galactocentric distance. They have also shown that the Galactocentric distance around 10kpc f_{dg} is around 0.6-0.8. The results in this thesis for f_{dg} are in good agreement with this that it is observed that as the spiral-arms subregions have high f_{dg} values which are around 7kpc away. Also, they have shown that the increase in f_{dg} is due to the different mean extinctions as the Galactic metallicity gradient influence the clouds with similar column densities in the inner and outer galaxy. At high resolutions, the mean extinction varies from subregion to subregion, which is why high f_{dg}.

Overall the results in this thesis are in reasonable agreement with the findings of observational and theoretical works.

Chapter 7

Conclusion

I have performed an investigation of CO-dark molecular gas fraction in the specific $10M_{\odot}$ resolution region of fiducial Milky Way model produced by Smith et al. (2020) (Figure 4.1). To produce this model Smith et al. (2020) have used a moving mesh AREPO code which includes a self-consistent treatment of interstellar medium chemistry and performed a high-resolution simulation in which a mass resolution of $4M_{\odot}$ is reached in the most highly refined portion of the simulation. The simulations are evolved for 261.1 Myr (which corresponds to the six spiral arm passages).

This thesis is carried out on the overall $10M_{\odot}$ resolution potential dominated region and its corresponding nine subregions at 50pc, 100pc, 250pc, 500pc, and 1kpc spatial resolutions. The desired spatial resolution is achieved by dividing the data and averaging the values over the pixels. Using equation 4.2 CO column density (N_{CO}), H_2 column density (N_{H_2}), HI column density (N_{HI}) and Total Column density (N_{SD}) are calculated, and their respective AREPO images are shown in the Figures 4.3, 4.4, 4.5 and 4.2.

CO (1-0) emission is determined by using equation 4.3. CO-dark gas fraction (f_{dg}) is estimated by considering the velocity integrated CO (1-0) intensity typical sensitivity limit (W_{CO}) less than 0.1 K kms^{-1} (4.6) and the threshold as $W_{CO,th} <$ 10 K kms^{-1} ($W_{CO,th}$ is the adopted boundary between CO-dark and CO-bright gas). CO-dark gas surrounds the CO-bright gas in the form of an envelope. At high resolutions, it is found that the standard assumed value of $W_{CO,th} < 10$ K kms^{-1} does not hold good for 50pc, 100pc and 250pc resolutions. i.e., the curve starts increasing and reaches f_{dg} value 1 before $W_{CO,th}$ (Figure 5.3). Considering the new $W_{CO,newth} < 1$ K kms^{-1} the total molecular mass between the sensitivity limit ($W_{CO} < 0.1$ K kms^{-1}) and $W_{CO,newth}$ is found to be only few percent. Hence, adopting this $W_{CO,newth}$ value the CO-dark gas fraction for the overall $10M_{\odot}$ resolution region 0.01 - 0.34, 0.15 - 0.32, 0.1 - 0.24, 0.22 and 0.36 for 50pc,

100pc, 250pc, 500pc, and 1kpc spatial resolutions respectively. Hence, one should consider $W_{CO,th}$ with care at different resolutions in order to determine the exact amount of H_2 mass in dark gas. It is found that at high spatial resolutions, more CO (1-0) emission is observed (see Figure5.2) compared to low spatial resolutions for all the subregions. By adopting the value of $W_{CO,th}$ < 10 K kms^{-1}, for the overall 10M$_\odot$ resolution region, CO-dark gas fraction is found to be 0.01 - 0.9 for 50pc spatial resolution, 0.15 - 0.9 for 100pc spatial resolution, 0.5 - 0.56 for 250pc spatial resolution, 0.22 for 500pc spatial resolution and 0.36 for 1kpc spatial resolution. For subregions f_{dg} is also found to vary along with the spatial resolutions (5.1).

An attempt to determine the relation between f_{dg} and the column densities for the overall 10M$_\odot$ resolution region has been made. When f_{dg} is plotted along the column densities, a huge scatter in the data is observed, which is highly sensitive to the spatial resolutions. As the spatial resolution is increased for each subregion which is initially 1kpc, the resolution is divided, and the data is averaged over the pixels. Thus, it is observed to consist of more data at high than low resolutions. For N_{CO} in the range 10^{15}-10^{17} cm^{-2} CO-dark gas fraction variation is observed. For N_{H_2} in the range $10^{18} - 10^{22}$ cm^{-2} the variation in CO-dark gas fraction is observed. For N_{HI} in the range 10^{20} cm^{-2} - 10^{22} cm^{-2} CO-dark gas is observed to vary. These are observed for all the spatial resolutions. No general trend is observed to estimate the relation between f_{dg} and column densities. Therefore, I have binned the column densities for $10^{0.5}$ cm^{-2} intervals and estimated the mean f_{dg} values in the binned column density values. The f_{dg} has both right and left-skewed data, and no general trend is observed over different resolutions. For a given N_{H_2} more CO is observed as the spatial resolution is increased, and at poor spatial resolutions, N_{H_2} data is obscured (Figure 5.6). For a given N_{HI} HI is observed at high values along with H_2 as the spatial resolution increases (Figures 4.4 and 4.5). At a given N_{sd} the fractional abundance of H_2 decreases as the spatial resolution increases (Figure 4.7). Hence, no co-relation is found for f_{dg} along with N_{H_2},N_{HI} and N_{sd} at different spatial resolutions are found by using this method.

The CO-H_2 conversion factor (X_{CO}) is calculated using equation 2.1 by considering the CO (1-0) integrated intensities of W_{CO} > 0.1 K kms^{-1}. For the overall 10M$_\odot$ resolution region the globally averaged X_{CO} is found to be 3.4 $\times$ 10^{20} cm^{-2}K^{-1}km^{-1}s for 50pc spatial resolution, 2.5 $\times$ 10^{20} cm^{-2}K^{-1}km^{-1}s for 100pc resolution, 1.4 $\times$ 10^{21} cm^{-2}K^{-1}km^{-1}s for 250pc resolution, 1.7 $\times$ 10^{20} cm^{-2}K^{-1}km^{-1}s for 500pc resolution and 1.9 $\times$ 10^{20} cm^{-2}K^{-1}km^{-1}s for 1kpc resolution. Globally averaged X_{CO} is found to be 1-3 orders of magnitude lower

than $X_{CO,gal}$, this is due to the obscuration of N_{H_2}. These X_{CO} values are close to the standard adopted Galactic value for Milky Way $X_{CO,gal} = 2.2 \times 10^{20}$ cm^{-2}K^{-1}km^{-1}s.

Finally, with the help of the above conclusions, I conclude that CO-dark gas fraction varies along with the observed spatial resolution of the AREPO image, which affects the estimation of the overall H_2 mass budget in a particular region.

Bibliography

Ballesteros-Paredes J., 2006, Monthly Notices of the RAS, 372, 443

Bauer A., Springel V., 2012, Monthly Notices of the Royal Astronomical Society, 423, 2558

Beck R., Wielebinski R., Oswalt T., Gilmore G., 2013, Dordrecht: Springer Science+ Business Media, 5, 641

Berger M. J., Colella P., 1989, Journal of computational Physics, 82, 64

Binney J., Tremaine S., 1987, Galactic dynamics

Bisbas T. G., Bell T. A., Viti S., Yates J., Barlow M. J., 2012, Monthly Notices of the RAS, 427, 2100

Bisbas T. G., Tan J. C., Tanaka K. E. I., 2021, Monthly Notices of the RAS, 502, 2701

Blitz L., 1993, in Levy E. H., Lunine J. I., eds, Protostars and Planets III. p. 125

Blitz L., Shu F. H., 1980, Astrophysical Journal, 238, 148

Bloemen J. B. G. M., et al., 1986, Astronomy and Astrophysics, 154, 25

Bolatto A. D., Wolfire M., Leroy A. K., 2013, Annual Review of Astron and Astrophys, 51, 207

Burgh E. B., France K., McCandliss S. R., 2007, Astrophysical Journal, 658, 446

Burton M., et al., 2013, arXiv e-prints, p. arXiv:1307.0712

Busch M. P., Allen R. J., Engelke P. D., Hogg D. E., Neufeld D. A., Wolfire M. G., 2019a, Astrophysical Journal, 883, 158

Busch M. P., Allen R. J., Engelke P. D., Hogg D. E., Neufeld D. A., Wolfire M. G., 2019b, Astrophysical Journal, 883, 158

Caldwell J., Ostriker J., 1981, The Astrophysical Journal, 251, 61

Cartagena A. F. I., 2020, PhD thesis, The University of Manchester (United Kingdom)

Cazaux S., Tielens A. G. G. M., 2002, Astrophysical Journal, Letters, 575, L29

Cazaux S., Tielens A. G. G. M., 2004, Astrophysical Journal, 604, 222

Christensen C., Quinn T., Governato F., Stilp A., Shen S., Wadsley J., 2012, Monthly Notices of the RAS, 425, 3058

Clark P. C., Glover S. C. O., Klessen R. S., 2012, Monthly Notices of the RAS, 420, 745

Clark P. C., Glover S. C. O., Ragan S. E., Duarte-Cabral A., 2019, Monthly Notices of the RAS, 486, 4622

Cox D. P., Gómez G. C., 2002, Astrophysical Journal, Supplement, 142, 261

Crutcher R. M., 2012, Annual Review of Astronomy and Astrophysics, 50, 29

Dabrowski I., 1984, Canadian Journal of Physics, 62, 1639

Dobbs C. L., Glover S. C. O., Clark P. C., Klessen R. S., 2008a, Monthly Notices of the RAS, 389, 1097

Dobbs C. L., Glover S. C. O., Clark P. C., Klessen R. S., 2008b, Monthly Notices of the RAS, 389, 1097

Draine B. T., 1978, Astrophysical Journal, Supplement, 36, 595

Draine B. T., 2011, Physics of the Interstellar and Intergalactic Medium

Escalante V., 1991, Publications of the ASP, 103, 838

Federman S. R., Glassgold A. E., Jenkins E. B., Shaya E. J., 1980, Astrophysical Journal, 242, 545

Gingold R. A., Monaghan J. J., 1977, Monthly notices of the royal astronomical society, 181, 375

Glover S. C. O., Abel T., 2008, Monthly Notices of the RAS, 388, 1627

Glover S. C. O., Clark P. C., 2012a, Monthly Notices of the RAS, 421, 9

Glover S. C. O., Clark P. C., 2012b, Monthly Notices of the RAS, 421, 116

Glover S. C. O., Clark P. C., 2012c, Monthly Notices of the RAS, 426, 377

Glover S. C. O., Mac Low M.-M., 2007a, Astrophysical Journal, Supplement, 169, 239

Glover S. C. O., Mac Low M.-M., 2007b, Astrophysical Journal, 659, 1317

Glover S. C. O., Mac Low M. M., 2011, Monthly Notices of the RAS, 412, 337

Glover S. C. O., Federrath C., Mac Low M. M., Klessen R. S., 2010, Monthly Notices of the RAS, 404, 2

Gnat O., Ferland G. J., 2012, Astrophysical Journal, Supplement, 199, 20

Gnedin N. Y., Tassis K., Kravtsov A. V., 2009a, Astrophysical Journal, 697, 55

Gnedin N. Y., Tassis K., Kravtsov A. V., 2009b, Astrophysical Journal, 697, 55

Goldsmith P. F., Heyer M., Narayanan G., Snell R., Li D., Brunt C., 2008, Astrophysical Journal, 680, 428

Goldsmith P. F., Velusamy T., Li D., Langer W. D., 2010, Astrophysical Journal, 715, 1370

Grenier I. A., Casandjian J.-M., Terrier R., 2005, Science, 307, 1292

Habing H. J., 1968, Bulletin Astronomical Institute of the Netherlands, 19, 421

Hall K. P., Stanimirović S., Lee M.-Y., Wolfire M., Goldsmith P.,

Hollenbach D., Kaufman M. J., Bergin E. A., Melnick G. J., 2009, Astrophysical Journal, 690, 1497

Hollenback D. J., McCray R., 1975, in Bulletin of the American Astronomical Society. p. 418

Hopkins P. F., Quataert E., Murray N., 2012, Monthly Notices of the Royal Astronomical Society, 421, 3488

Islam F., 2010, PhD thesis, UCL, United Kingdom

Kalberla P. M. W., Burton W. B., Hartmann D., Arnal E. M., Bajaja E., Morras R., Pöppel W. G. L., 2005, Astronomy and Astrophysics, 440, 775

Kalberla P. M. W., Kerp J., Haud U., 2020, Astronomy and Astrophysics, 639, A26

Kwok S., 2007, Physics and chemistry of the interstellar medium. University Science Books

Langer W. D., Velusamy T., Pineda J. L., Goldsmith P. F., Li D., Yorke H. W., 2010a, Astronomy and Astrophysics, 521, L17

Langer W. D., Velusamy T., Pineda J. L., Goldsmith P. F., Li D., Yorke H. W., 2010b, Astronomy and Astrophysics, 521, L17

Leroy A., Bolatto A., Stanimirovic S., Mizuno N., Israel F., Bot C., 2007, Astrophysical Journal, 658, 1027

Li D., et al., 2018, Astrophysical Journal, Supplement, 235, 1

Liszt H. S., Lucas R., 1998, Astronomy and Astrophysics, 339, 561

Liszt H. S., Pety J., 2012, Astronomy and Astrophysics, 541, A58

Lombardi M., Alves J., Lada C. J., 2006, Astronomy and Astrophysics, 454, 781

Lucy L., 1977, A numerical approach to the testing of the fission hypothesis. aj, 82: 1013–1024

Luisi M., 2019, The Impact of HII Regions on the Interstellar Medium of our Galaxy. West Virginia University

Luo G., et al., 2020, Astrophysical Journal, Letters, 889, L4

McMillan P. J., 2017a, Monthly Notices of the RAS, 465, 76

McMillan P. J., 2017b, Monthly Notices of the RAS, 465, 76

Nelson R. P., Langer W. D., 1997, Astrophysical Journal, 482, 796

Nieten C., Neininger N., Guélin M., Ungerechts H., Lucas R., Berkhuijsen E. M., Beck R., Wielebinski R., 2006, Astronomy and Astrophysics, 453, 459

Offner S. S. R., Bisbas T. G., Viti S., Bell T. A., 2013, Astrophysical Journal, 770, 49

Pakmor R., Springel V., Bauer A., Mocz P., Munoz D. J., Ohlmann S. T., Schaal K., Zhu C., 2016, Monthly Notices of the RAS, 455, 1134

Paradis D., Dobashi K., Shimoikura T., Kawamura A., Onishi T., Fukui Y., Bernard J. P., 2012, Astronomy and Astrophysics, 543, A103

Pen U.-L., 1998, The Astrophysical Journal Supplement Series, 115, 19

Pilbratt G. L., et al., 2010, Astronomy and Astrophysics, 518, L1

Pineda J. E., Caselli P., Goodman A. A., 2008, Astrophysical Journal, 679, 481

Pineda J. L., Langer W. D., Velusamy T., Goldsmith P. F., 2013, Astronomy and Astrophysics, 554, A103

Planck Collaboration et al., 2011a, Astronomy and Astrophysics, 536, A19

Planck Collaboration et al., 2011b, Astronomy and Astrophysics, 536, A19

Price D. J., 2008, Journal of Computational Physics, 227, 10040

Pringle J. E., Allen R. J., Lubow S. H., 2001, Monthly Notices of the RAS, 327, 663

Reed B. C., 2000, Astronomical Journal, 120, 314

Savage B. D., Bohlin R. C., Drake J. F., Budich W., 1977, Astrophysical Journal, 216, 291

Schöier F. L., van der Tak F. F. S., van Dishoeck E. F., Black J. H., 2005, Astronomy and Astrophysics, 432, 369

Scoville N. Z., Yun M. S., Clemens D. P., Sanders D. B., Waller W. H., 1987, Astrophysical Journal, Supplement, 63, 821

Sheffer Y., Rogers M., Federman S. R., Abel N. P., Gredel R., Lambert D. L., Shaw G., 2008, Astrophysical Journal, 687, 1075

Shetty R., Glover S. C., Dullemond C. P., Klessen R. S., 2011, Monthly Notices of the RAS, 412, 1686

Sijacki D., Vogelsberger M., Kereš D., Springel V., Hernquist L., 2012, Monthly Notices of the Royal Astronomical Society, 424, 2999

Slyz A., Prendergast K. H., 1999, Astronomy and Astrophysics Supplement Series, 139, 199

Smith R. J., Glover S. C. O., Clark P. C., Klessen R. S., Springel V., 2014, Monthly Notices of the RAS, 441, 1628

Smith R. J., et al., 2020, Monthly Notices of the RAS, 492, 1594

Spitzer L., 1998, Physical Processes in the Interstellar Medium

Springel V., 2010a, Monthly Notices of the Royal Astronomical Society, 401, 791

Springel V., 2010b, Monthly Notices of the RAS, 401, 791

Stone J. M., Norman M. L., 1992, Astrophysical Journal Supplement Series (ISSN 0067-0049), vol. 80, no. 2, June 1992, p. 753-790. Research supported by University of Illinois., 80, 753

Strong A. W., Mattox J. R., 1996, Astronomy and Astrophysics, 308, L21

Tasker E. J., Brunino R., Mitchell N. L., Michielsen D., Hopton S., Pearce F. R., Bryan G. L., Theuns T., 2008, Monthly Notices of the Royal Astronomical Society, 390, 1267

Tielens A. G. G. M., 2010, The Physics and Chemistry of the Interstellar Medium

Tielens A. G. G. M., Hollenbach D., 1985, Astrophysical Journal, 291, 722

Wadsley J., Veeravalli G., Couchman H., 2008, Monthly Notices of the Royal Astronomical Society, 387, 427

Wolfire M. G., Tielens A. G. G. M., Hollenbach D., Kaufman M. J., 2008, Astrophysical Journal, 680, 384

Wolfire M. G., Hollenbach D., McKee C. F., 2010, Astrophysical Journal, 716, 1191

Xu G., 1997, Monthly Notices of the Royal Astronomical Society, 288, 903

de Graauw, Th. et al., 2010, A&A, 518, L6

den Brok J. S., et al., 2021, Monthly Notices of the RAS, 504, 3221